





Article

Feasibility of Estimating Turbulent Heat Fluxes via Variational Assimilation of Reference-Level Air Temperature and Specific Humidity Observations

Elahe Tajfar ¹, Sayed M. Bateni ¹, Essam Heggy ^{2,3} and Tongren Xu ^{4,*}

¹ Department of Civil and Environmental Engineering and Water Resources Research Center, University of Hawaii at Manoa, Honolulu, HI 96822, USA; etajfar@hawaii.edu (E.T.); smbateni@hawaii.edu (S.M.B.)

² Viterbi School of Engineering, University of Southern California, Los Angeles, CA 90089, USA; heggy@usc.edu

³ Jet Propulsion Laboratory, California Institute of Technology, Pasadena, CA 91109, USA

⁴ State Key Laboratory of Earth Surface Processes and Resource Ecology, School of Natural Resources, Faculty of Geographical Science, Beijing Normal University, Beijing 100875, China

* Correspondence: xutr@bnu.edu.cn

Received: 21 February 2020; Accepted: 23 March 2020; Published: 26 March 2020



Abstract: This study investigated the feasibility of partitioning the available energy between sensible (H) and latent (LE) heat fluxes via variational assimilation of reference-level air temperature and specific humidity. For this purpose, sequences of reference-level air temperature and specific humidity were assimilated into an atmospheric boundary layer model (ABL) within a variational data assimilation (VDA) framework to estimate H and LE . The VDA approach was tested at six sites (namely, Arou, Audubon, Bondville, Brookings, Desert, and Willow Creek) with contrasting climatic and vegetative conditions. The unknowns of the VDA system were the neutral bulk heat transfer coefficient (C_{HN}) and evaporative fraction (EF). EF estimates were found to agree well with observations in terms of magnitude and day-to-day fluctuations in wet/densely vegetated sites but degraded in dry/sparsely vegetated sites. Similarly, in wet/densely vegetated sites, the variations in the C_{HN} estimates were found to be consistent with those of the leaf area index (LAI) while this consistency deteriorated in dry/sparsely vegetated sites. The root mean square errors (RMSEs) of daily H and LE estimates at the Arou site (wet) were $25.43 \text{ (Wm}^{-2}\text{)}$ and $55.81 \text{ (Wm}^{-2}\text{)}$, which are respectively 57.6% and 45.4% smaller than those of $60.00 \text{ (Wm}^{-2}\text{)}$ and $102.21 \text{ (Wm}^{-2}\text{)}$ at the Desert site (dry). Overall, the results show that the VDA system performs well at wet/densely vegetated sites (e.g., Arou and Willow Creek), but its performance degrades at dry/slightly vegetated sites (e.g., Desert and Audubon). These outcomes show that the sequences of reference-level air temperature and specific humidity have more information on the partitioning of available energy between the sensible and latent heat fluxes in wet/densely vegetated sites than dry/slightly vegetated sites.

Keywords: turbulent heat fluxes; available energy; variational data assimilation; air temperature; specific humidity

1. Introduction

The accurate estimation of sensible (H) and latent (LE) heat fluxes is of vital importance in different disciplines, such as meteorology, ecology, agronomy, and hydrology [1,2]. Turbulent heat fluxes (H and LE) can be measured by different approaches, such as lysimeter, eddy-covariance station, Bowen ratio, and large-aperture scintillometer [3–7]. However, measurements of turbulent heat fluxes are difficult and costly, and therefore are available from a handful of sparse flux tower networks (e.g., Fluxnet, AsiaFlux, EuroFlux, AmeriFlux, etc.), and field experiments (e.g., Bushland

Evapotranspiration and Agricultural Remote Sensing Experiment 2008 (BEAREX08), Heihe Watershed Allied Telemetry Experimental Research (HiWATER), and First International Satellite Land Surface Climatology Project (ISLSCP) Field Experiment (FIFE), etc.) [8–11]. Consequently, different approaches have been developed to estimate turbulent heat fluxes [12–16].

In general, there are five major groups of studies for estimating turbulent heat fluxes. The first group, known as the triangle method, estimates latent heat flux by using empirical relations between land surface temperature (LST) and vegetation indices (VIs) [17–27]. A number of triangle methods also use spectral mixture analysis (SMA) to relate the radiometric temperature to subpixel fractions of substrate (S), vegetation (V), and dark (D) spectral endmembers to estimate LE [28]. In the second group, the diagnostic method, the surface energy balance (SEB) equation is solved using instantaneous measurements of LST and micrometeorological data [29–35]. The third group, the combination method, predicts turbulent heat fluxes by incorporating the LST observations into the Penman–Monteith equation [36–38]. The fourth group, the land data assimilation system (LDAS), estimates turbulent heat fluxes by the ensemble Kalman filter (EnKF) approach [39–44].

The fifth group, the variational data assimilation (VDA) method, retrieves turbulent heat fluxes by assimilating sequences of LST observations into the force-restore and/or heat diffusion equation [10,45–56]. In these studies, the implicit information in the sequences of LST observations is used to partition the available energy between the sensible and latent heat fluxes. The performance of these VDA approaches degrades in wet and/or heavily vegetated sites [57,58]. This occurs because in these sites, evapotranspiration is at stage-I (energy limited), and is mainly controlled by the state variables of the atmosphere (i.e., air temperature and humidity) and not LST. These VDA approaches also require the specification of soil thermal conductivity and heat capacity as well as the deep soil temperature, which are typically unavailable. Several studies [59,60] enhanced the performance of VDA approaches by assimilating soil moisture or the antecedent precipitation index (API). Following these VDA studies, Bateni and Entekhabi [42] analytically showed that the sequences of LST observations have information on the relative efficiency of surface energy balance components.

In a departure from the use of sequences of LST measurements, several studies showed that the reference-level air temperature and humidity measurements contain useful information about soil moisture [61–71] and turbulent heat fluxes [72–80]. However, these studies mostly require the specification of surface roughness lengths for heat and momentum as well as ground heat flux, which are often unavailable.

Given the abovementioned shortcomings of the existing VDA approaches, Tajfar et al. [81] developed a VDA approach that estimates H and LE by assimilating sequences of reference-level air temperature and specific humidity (i.e., state variables of the atmosphere) into an atmospheric boundary layer (ABL) model. The main unknowns of the Tajfar et al. [81] VDA approach are the neutral bulk heat transfer coefficient (C_{HN}) (that scales the sum of H and LE) and evaporative fraction (EF) (that scales the partitioning of available energy between H and LE). Tajfar et al. [81] tested their VDA approach only at a grass-dominated sub-humid site in Kansas, and showed that sequences of the reference-level air temperature and specific humidity have implicit information for constraining C_{HN} and EF , and retrieving turbulent heat fluxes.

In this study, the VDA approach of Tajfar et al. [81] was tested at six sites to assess how much information is contained in the sequences of reference-level air temperature and specific humidity for estimating sensible and latent heat fluxes in contrasting vegetative and climatic conditions. If the reference-level air temperature and specific humidity measurements have sufficient information, the C_{HN} and EF , and consequently the turbulent heat fluxes estimates from the VDA approach, will be close to their true values. If these measurements do not have enough information, the C_{HN} , EF , H , and LE estimates will be poor.

This paper is structured as follows. Section 2 explains the methodology, including the surface energy balance (SEB) equation, the ABL model, and the VDA scheme. Section 3 describes the study sites. The results are given in Section 4. Finally, conclusions are reported in Section 5.

2. Materials and Methods

2.1. Sensible and Latent Heat Fluxes

The sensible heat flux is given by:

$$H = \rho c_p C_{HN} f(Ri) U (T - T_a), \quad (1)$$

where ρ is the air density, c_p is the specific heat capacity of air, U is the wind speed at the reference level ($z_{ref} = 2 \text{ m}$), T is the land surface temperature, T_a is the air temperature at z_{ref} , and f is the atmospheric stability correction function, which is a function of the Richardson number (Ri). Ri is a measure of atmospheric stability. The stability correction function (f) proposed by Caparrini et al. [45] performed well in previous studies [49–51,53,57,81–83], and thus was used in this study. It is given by $f(Ri) = 1 + 2(1 - e^{10Ri})$. C_{HN} is the first unknown of the VDA approach, which depends on the characteristics of the landscape, and is assumed to be constant during each month [49,50,53,57]. C_{HN} is mainly a function of LAI and to a lesser extent wind speed, friction velocity, solar elevation, and the structure and shape of vegetation (i.e., crown density and vertical distribution of foliage elements) [50,84–88].

EF is the second unknown of the VDA approach that represents partitioning between the turbulent heat fluxes, and is defined as the ratio of latent heat flux to the sum of turbulent heat fluxes:

$$EF = \frac{LE}{LE + H}. \quad (2)$$

Crago [89], Caparrini et al. [46,47], and Bateni et al. [49–51] showed that EF is almost constant for near-peak radiation hours [09:00–16:00 LT] on days without precipitation. To estimate LE , Equation (2) can be re-written as follows:

$$LE = \frac{EF}{1 - EF} H. \quad (3)$$

It is worth mentioning that the assumption of daily constant EF and monthly constant C_{HN} are widely used in VDA studies [42,44,46,47,49,50,53,55,56,81–83] to estimate H and LE .

2.2. Atmospheric Boundary Layer (ABL) Model

A mixed-layer model, which performs well compared to the complicated large eddy simulation models, is used to simulate ABL processes [81–83,90,91]. The profiles of potential temperature (θ) and specific humidity (q) are assumed to be constant with height throughout the mixed layer. As shown in Figure 1, the thin layer between the ground and the mixed layer is called the surface layer (SL). The surface layer is assumed to be 10% of the mixed-layer top, h (i.e., $z_{SL} = 0.1h$), and is convectively unstable during the growth phase of the boundary layer [73,79,81,83].

2.2.1. Energy and Moisture Budget Equations

The potential temperature and specific humidity in the mixed layer are given by:

$$\rho c_p h \frac{d\theta}{dt} = (R_{ad} + R_{gu}) \varepsilon_m - R_{Ad} - R_{Au} + H + H_{top}, \quad (4)$$

$$\rho h L_v \frac{dq}{dt} = LE + LE_{top}, \quad (5)$$

where H_{top} and LE_{top} are the entrainment sensible and latent heat fluxes from above the mixed layer, respectively; ε_m is the mixed-layer bulk emissivity; t is the time; and L_v is the latent heat of vaporization. R_{ad} and R_{gu} are the downward longwave radiation from the free atmosphere and upward longwave radiation from the ground into the mixed layer, respectively. R_{Ad} and R_{Au} are the downward and upward longwave radiative fluxes from within the mixed layer, respectively.

The potential temperature at the level of 1000 mb (i.e., θ_a) is obtained from the reference-level air temperature (T_a) via $\theta_a = T_a(P_0/P_s)^{R_d/c_p}$ (where R_d is the gas constant of dry air, P_s is the surface pressure, and P_0 is 1000 mb) [92]. The variations of the potential temperature and specific humidity profiles within the surface layer can be explained by the Monin–Obukhov similarity theory (MOST) [78,93]. Hence, θ_{SL} and q_{SL} are found from θ_a and q_a using the MOST (see Appendix B). As q and θ are uniform throughout the mixed layer, the initial conditions for Equations (4) and (5) (i.e., $\theta(t = t_o)$ and $q(t = t_o)$) are set to be equal to $\theta_{SL}(t = t_o)$ and $q_{SL}(t = t_o)$, respectively.

2.2.2. Radiative Fluxes

The downwelling longwave radiation from the overlying atmosphere (R_{ad}) and the upwelling longwave radiative flux from the land surface beneath (R_{gu}) are given by:

$$R_{ad} = \varepsilon_{ad}\sigma T_{h+}^4, \quad (6)$$

$$R_{gu} = \varepsilon_s\sigma T^4, \quad (7)$$

where σ is the Stefan–Boltzman constant, ε_{ad} is the effective emissivity above the mixed layer [73,81,83,94–96], T_{h+} is the air temperature exactly above the mixed layer [95,96], and ε_s is the surface emissivity.

The downward and upward longwave radiative fluxes from within the mixed layer (R_{Ad} and R_{Au}) are presented by:

$$R_{Ad} = \varepsilon_d\sigma\theta^4, \quad (8)$$

$$R_{Au} = \varepsilon_u\sigma\theta^4, \quad (9)$$

where ε_d and ε_u are the mixed-layer downward and upward emissivity, respectively [95,96].

2.2.3. Mixed-Layer Height

The daytime ABL height growth is calculated by [81,83,95–99]:

$$\frac{dh}{dt} = \frac{2(G_* - D_1 - D_2)\theta}{gh\delta_\theta} + \frac{H_v}{\rho c_p \delta_\theta}, \quad (10)$$

where the various terms in Equation (10) are given by:

$$G_* = u_{SL}u_*^2, \quad (11)$$

$$D_1 = u_{SL}u_*^2(1 - e^{-\varphi h}), \quad (12)$$

$$D_2 = 0.4\left(\frac{gh}{\theta} \frac{H_v}{\rho c_p}\right), \quad (13)$$

$$H_v = H + 0.61\theta c_p E \approx H + 0.07LE, \quad (14)$$

where u_* is the friction velocity; u_{SL} is the wind speed at the top of the surface layer, which is obtained from the reference-level wind speed (U) via the MOST (the readers are referred to Appendix B); G_* is the production of mechanical turbulent energy; g is gravitational acceleration; φ is the mechanical turbulence dissipation parameter, which is set to 0.01 [73,81,83,96,99]; H_v is the virtual heat flux at the surface; E is the rate of evaporation from ground; and δ_θ is the potential temperature inversion strength at the top of the mixed layer.

2.2.4. Inversion Strengths of θ and q

There are instantaneous jumps (inversion strengths) in temperature and humidity (δ_θ and δ_q) at the top of the mixed layer (Figure 1). As shown in Equation (15), the inversion strength of θ increases

as the boundary layer grows, but it decreases as the boundary layer warms up. Similarly, the inversion strength of q increases as the boundary layer develops, and it increases (becomes more negative) as the boundary layer becomes moister (Equation (16)). The magnitudes of these jumps can be calculated by the following prognostic equations [81,83,100]:

$$\frac{d\delta_\theta}{dt} = \gamma_\theta \frac{dh}{dt} - \frac{d\theta}{dt}, \quad (15)$$

$$\frac{d\delta_q}{dt} = \gamma_q \frac{dh}{dt} - \frac{dq}{dt}, \quad (16)$$

where γ_θ and γ_q are the lapse rates in the potential temperature and specific humidity above the mixed layer.

2.2.5. Entrainment Fluxes

As the boundary layer grows, warm dry air from the free atmosphere enters the mixed layer, and results in the presence of sensible and latent heat fluxes entrainment (H_{top} and LE_{top}). H_{top} heats up the ABL and LE_{top} reduces its humidity [101]:

$$H_{top} = AH, \quad (17)$$

$$LE_{top} = \rho L_v \delta_q \frac{dh}{dt}. \quad (18)$$

A typical value of 0.2 is used for A [81,83,90,91].

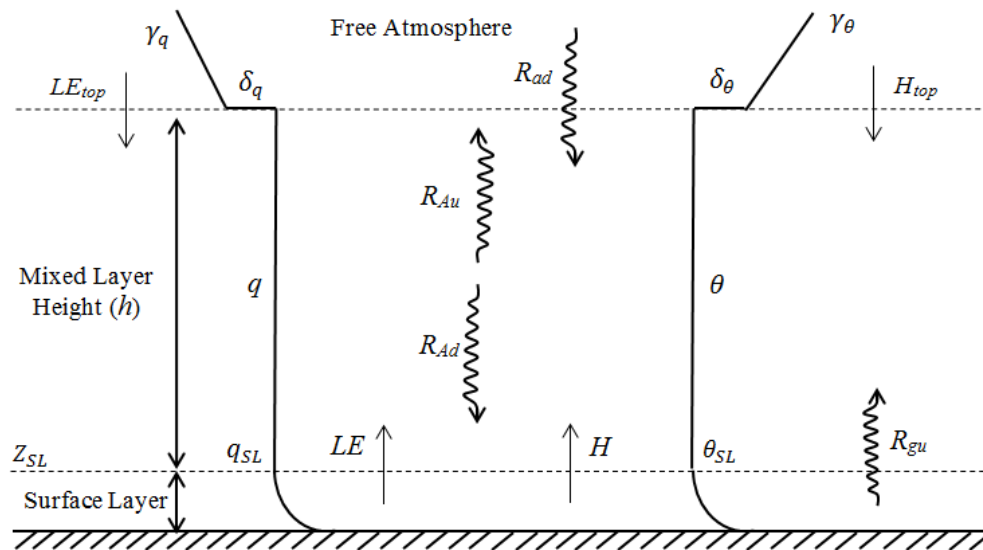


Figure 1. Idealized profiles of the potential temperature (θ) and specific humidity (q) in the atmospheric boundary layer (ABL), and corresponding fluxes.

2.3. Variational Data Assimilation (VDA) Approach

The unknowns of the VDA system (i.e., C_{HN} and EF) are obtained by minimizing the objective function J . Two different integral time scales are used in the objective function J . The first one covers the entire assimilation period in which C_{HN} is assumed to be constant ($N = 30$ days). The second time scale

constitutes the assimilation window in which EF is presumed to be constant $[t_0, t_1] = [09:00-16:00 \text{ LT}]$. The objective function J is expressed as:

$$\begin{aligned}
 J(\theta, q, \lambda_1, \lambda_2, R, EF) = & \sum_{i=1}^N \int_{t_0}^{t_1} [\theta_i(t) - \theta_{SL,i}(t)]^T R_{\theta}^{-1} [\theta_i(t) - \theta_{SL,i}(t)] dt \\
 & + \sum_{i=1}^N \int_{t_0}^{t_1} [q_i(t) - q_{SL,i}(t)]^T R_q^{-1} [q_i(t) - q_{SL,i}(t)] dt \\
 & + (R - R')^T B_R^{-1} (R - R') \\
 & + \sum_{i=1}^N (EF_i - EF'_i)^T B_{EF}^{-1} (EF_i - EF'_i) \\
 & + \sum_{i=1}^N \int_{t_0}^{t_1} \lambda_{1i}(t) \left[\rho c_p h_i(t) \frac{d\theta_i(t)}{dt} - (R_{ad} + R_{gu}) \varepsilon_m + R_{Ad} + R_{Au} - H - H_{top} \right] dt \\
 & + \sum_{i=1}^N \int_{t_0}^{t_1} \lambda_{2i}(t) \left[\rho h_i(t) L_v \frac{dq_i(t)}{dt} - LE - LE_{top} \right] dt.
 \end{aligned} \tag{19}$$

The first term in the right-hand side of Equation (19) is the quadratic of difference between the top of the surface layer potential temperature (θ_{SL}) and the ABL potential temperature (θ) estimates from Equation (4). Similarly, the second term is the quadratic of the misfit between the top of the surface layer specific humidity (q_{SL}) and the ABL specific humidity (q) estimates from Equation (5). Using the MOST (see Appendix B), θ_{SL} and q_{SL} are retrieved from the reference-level air temperature (T_a) and specific humidity (q_a), respectively. To make C_{HN} strictly positive, it is transformed to R via $C_{HN} = e^R$. The third and fourth terms are the quadratic errors of the unknown parameters (i.e., R and EF) with respect to their prior values (R' and EF'). The last two terms are the physical constraints adjoined to the model through the Lagrange multipliers λ_1 and λ_2 . R_{θ}^{-1} and R_q^{-1} are the inverse error covariance matrices of θ and q , respectively. B_R^{-1} and B_{EF}^{-1} are the inverse background error covariance matrices of R and EF , respectively. Following Tajfar et al. [81,83], the diagonal elements of R_{θ}^{-1} , R_q^{-1} , B_R^{-1} , and B_{EF}^{-1} are set to 10^{-1} K^{-2} , $10^5 \text{ (kg/kg)}^{-2}$, 10^8 , and 10^9 , respectively.

To minimize the objective function, its first variation (δJ) with respect to the independent variables θ , q , λ_1 , λ_2 , R , and EF is set to zero. This leads to a set of the so-called Euler–Lagrange equations that should be solved simultaneously. The Euler–Lagrange equations are presented in Appendix C.

3. Study Sites

The ability of the VDA approach to partition the available energy between the turbulent heat fluxes was tested at six sites (namely, Arou, Audubon, Bondville, Brookings, Desert, and Willow Creek) with contrasting climatic and vegetative conditions. Audubon, Bondville, Brookings, and Willow Creek are located in the United States (Figure 2). Arou and Desert are situated in the middle reach of Heihe River basin (HRB) in the Gobi desert in Northern China (<http://card.westgis.ac.cn/>) (Figure 3). Audubon (in Arizona) is a grassland water-limited monsoonal site with a temperate arid climate (<https://ameriflux.lbl.gov/sites/siteinfo/US-Aud>). Bondville (in Illinois) is a cropland that has a humid continental climate with hot summers (<https://ameriflux.lbl.gov/sites/siteinfo/US-Bo1>). Brookings (in South Dakota) is a grassland with a temperate continental climate and no dry season (<https://ameriflux.lbl.gov/sites/siteinfo/US-Bkg>). Willow Creek (in Wisconsin) is a deciduous broad-leaf forest with dense vegetation cover and significant precipitation (<https://ameriflux.lbl.gov/sites/siteinfo/US-WCr>). Arou (in Qinghai) is a dense grassland with high soil moisture (<http://data.tpdac.ac.cn/en/data/9074b105-549c-4f15-b8a5-87602a45134d/>). Desert (in Inner Mongolia) is barren soil and has low precipitation and sparse canopy cover (<http://data.tpdac.ac.cn/en/data/77c7bfd5-38d3-41e2-93ce-cb4d8c0d475a/>). Leaf area index (LAI) ranges from 0.00 in Desert (barren land) to 5.67 in Willow Creek (dense forest). Soil moisture (SM) varies from 0.03 in Desert (dry) to 0.36 in Arou (wet). These sites were chosen to sample different land cover types (forest, grassland, cropland, and barren land), and cover a wide range of vegetation density and soil moisture conditions (Table 1).



Figure 2. Locations of the four study sites (i.e., Audubon, Brookings, Bondville, and Willow Creek) in the United States.



Figure 3. Location of the two study sites (i.e., Arou and Desert) in the Gobi Desert in China.

Table 1. Environmental characteristics of the study sites.

Site	Year	DOY	Latitude	Longitude	Vegetation Type	SM*	LAI*	Elevation (m)
Arou, China	2015	170–259	38.0473°N	100.4643°E	Grassland	0.36	3.57	3033
Willow Creek, WI	2005	170–259	45.8059°N	90.0799°W	Forest	0.22	5.67	520
Brookings, SD	2009	176–265	44.3453°N	96.8362°W	Grassland	0.29	1.72	510
Bondville, IL	2005	182–271	40.0062°N	88.2904°W	Cropland	0.16	2.24	219
Audubon, AZ	2006	170–259	31.5907°N	110.5092°W	Grassland	0.12	0.54	1469
Desert, China	2015	170–259	42.1100°N	100.9900°E	Barren land	0.03	0	1000

* LAI and SM represent respectively the mean leaf area index ($\text{m}^2 \text{m}^{-2}$) and soil moisture ($\text{m}^3 \text{m}^{-3}$) over the modeling periods. WI: Wisconsin, AZ: Arizona, IL: Illinois, and SD: South Dakota.

LAI and SM are the key factors affecting the partitioning of available energy between the sensible and latent heat fluxes [50,58,102]. Hence, testing the VDA approach at the abovementioned six sites provides insights into how much information is contained in the sequences of reference-level air temperature and specific humidity for partitioning the available energy between H and LE in various climatic and vegetative conditions.

Soil moisture and half-hourly meteorological data (air temperature and specific humidity, wind speed, and atmospheric pressure) at the Audubon, Bondville, Brookings, and Willow Creek sites were retrieved from the AmeriFlux archive (<http://www.ameriflux.lbl.gov>). The sensible and latent heat fluxes at these sites were measured by eddy covariance (EC) stations, and are available on the Ameriflux database. LAI data were obtained from the Global LAnd Surface Satellites (GLASS) product [103,104]. This product is accessible on the University of Maryland global land cover facility archive (<http://www.un-spider.org/links-and-resources/data-sources/global-land-cover-facility-university-maryland-nasagofc-gold>).

The Multiscale Observation Experiment on Evapotranspiration over the Heihe Watershed Allied Telemetry Experimental Research (HiWATER-MUSOEXE) provides half-hourly measurements of wind speed, air temperature, soil moisture, relative humidity, and pressure at the Arou and Desert sites (<http://card.westgis.ac.cn/hiwater>) [9,11,105,106]. The sensible and latent heat fluxes were recorded at these sites by an EC station every 30 min (<http://card.westgis.ac.cn/data/e9e38ff4-5a10-4977-9de7-61e9c25bd333>). LAI data at the Arou and Desert sites were also obtained from the GLASS product. Vegetation height was obtained by in situ measurements [105].

The initial condition for h is required to solve Equation (10). Similarly, the initial conditions for δ_θ and δ_q , and the magnitudes of γ_θ and γ_q are needed to integrate Equations (15) and (16) forward in time. Following Tajfar et al. [81,83], the initial conditions for h , δ_θ , and δ_q , and the magnitudes of γ_θ and γ_q were varied from 100 to 500 m, 2 to 6 K, -4.8×10^{-3} to $-0.5 \times 10^{-3} \text{ kg kg}^{-1}$, 2 to 8 K km^{-1} , and -7×10^{-3} to $-0.5 \times 10^{-3} \text{ kg kg}^{-1} \text{ km}^{-1}$ with the increment of 100 m, 0.4 K, $0.4 \times 10^{-3} \text{ kg kg}^{-1}$, 0.5 K km^{-1} , and $0.5 \times 10^{-3} \text{ kg kg}^{-1} \text{ km}^{-1}$, respectively. For each study site, the magnitudes of $h(t = t_0)$, $\delta_\theta(t = t_0)$, and $\delta_q(t = t_0)$, γ_θ , and γ_q that lead to a minimum cost function (J) are reported in Table 2.

Table 2. The magnitudes of the initial conditions for h , δ_θ , and δ_q , as well as γ_θ and γ_q for the study sites.

Site	$h(t_0)$ (m)	$\delta_\theta(t_0)$ (K)	$\delta_q(t_0)$ (kg kg^{-1})	γ_θ (K km^{-1})	γ_q ($\text{kg kg}^{-1} \text{ km}^{-1}$)
Arou	400	4.5	-2.9×10^{-3}	5.7	-1.2×10^{-3}
Willow Creek	400	4.4	-3.2×10^{-3}	5.5	-1.5×10^{-3}
Brookings	400	4.0	-2.0×10^{-3}	4.5	-0.5×10^{-3}
Bondville	400	4.0	-4.0×10^{-3}	4.5	-3.0×10^{-3}
Audubon	400	2.8	-4.4×10^{-3}	3.0	-4.0×10^{-3}
Desert	400	2.4	-4.4×10^{-3}	3.0	-4.5×10^{-3}

The VDA was applied to the Desert (DOYs 170–259, 2015), Audubon (DOYs 170–259, 2006), Bonville (DOYs 182–271, 2005), Brookings (DOYs 176–265, 2009), Willow Creek (DOYs 170–259, 2005),

and Arou (DOYs 170–259, 2015). These modeling periods were chosen because they have a minimum data gap in H and LE measurements. Linear interpolation was used to fill the data gap [107,108].

4. Results and Discussions

As mentioned previously, C_{HN} and EF are the two key unknowns of the VDA system. Table 3 shows the estimated C_{HN} values from the VDA approach and corresponding LAI values at the six study sites. C_{HN} is mainly affected by vegetation phenology [44,46,47,50,52,55]. As shown in Table 3, the variations in C_{HN} estimates are consistent with those of LAI in the wet and/or densely vegetated sites. For instance, at the Willow Creek site, C_{HN} and LAI decrease slightly during the modeling periods. At the Arou and Brookings sites, C_{HN} reaches its highest value in the second monthly period and decreases in the third month. A similar trend is observed in LAI. At the Bondville site, the LAI and C_{HN} estimates remain almost constant during the modeling periods (DOYs 182–271).

The consistency between the C_{HN} retrievals and LAI weakens in dry/sparsely vegetated sites. At Audubon, LAI values increase continuously during the modeling periods. However, C_{HN} estimates decrease slightly in the second monthly period. At the Desert site, LAI is invariant, while C_{HN} shows slight variations in different assimilation periods. Among the study sites, Desert has the lowest C_{HN} estimates because it has no vegetation (LAI = 0), while Willow Creek has the highest C_{HN} values due to its dense vegetation cover (LAI = 5.67). In general, the study sites with higher LAI values (e.g., Arou and Willow Creek) have higher C_{HN} estimates compared to the sites with lower LAI (e.g., Desert and Audubon).

Overall, the results show that the C_{HN} estimates agree well with the vegetation phenology at wet and/or densely vegetated sites, although no information on vegetation density is used in the VDA approach. These findings indicate that the VDA approach can extract the implicit information contained in the air temperature and specific humidity measurements to estimate C_{HN} at wet and/or densely vegetated sites, but its performance degrades in dry and/or slightly vegetated sites.

Table 3. Estimated neutral bulk heat transfer coefficient (C_{HN}) values by the VDA approach at the six study sites, and corresponding LAI values.

Site	DOY	C_{HN}	LAI
Arou	170–199	0.0102	2.97
	200–229	0.0325	4.41
	230–259	0.0261	3.35
Willow Creek	170–199	0.0245	5.87
	200–229	0.0242	5.84
	230–259	0.0222	5.29
Brookings	176–206	0.0054	1.93
	207–237	0.0102	2.15
	238–265	0.0048	1.07
Bondville	182–211	0.0130	2.23
	212–241	0.0150	2.24
	242–271	0.0140	2.24
Audubon	170–199	0.0031	0.27
	200–229	0.0029	0.57
	230–259	0.0033	0.77
Desert	170–199	0.0022	0
	200–229	0.0020	0
	230–259	0.0010	0

Figure 4 shows the time series of EF estimates at the six study sites. EF values from the measured H and LE are also shown by open circles in Figure 4. The EF retrievals agree well with the observations in terms of both the magnitude and day-to-day fluctuations in wet and/or densely vegetated sites (e.g.,

Arou and Willow Creek). At these sites, the EF values are consistent with the wetting and dry down events, although no information on rainfall is used in the VDA approach. For example, sharp jumps are seen in the EF estimates after rainfall events at the Willow Creek site (e.g., DOY 181, 201, 206, 209, 221, 231, and 255), followed by reductions in the EF estimates during dry down events (e.g., DOY 171, 234, 245, 249, and 252). This shows that the sequences of air temperature and humidity have a significant amount of information on the partitioning of available energy between the turbulent heat fluxes in wet and/or densely vegetated sites.

The drying rate of land surface is controlled by both land surface properties and atmospheric factors [109]. At dry/sparsely vegetated sites (e.g., Desert and Audubon), evapotranspiration is at its second stage (water limited), and thus is mainly controlled by the land state variable (i.e., LST) rather than the atmospheric state variables (i.e., air temperature and specific humidity). Consequently, the coupling between EF and the atmospheric state variables is weak, and the retrieval of EF from air temperature and specific humidity becomes more uncertain. The Desert site is dry on DOYs 170–245. In this period, the VDA approach performs poorly and the EF estimate show unreasonable spikes. Towards the end of the modeling period (i.e., DOYs 246–259), the Desert site becomes wet due to rainfall events, and the EF estimates can capture the variations in the observations. Similarly, the Audubon site is mostly dry on DOYs 170–210, and thus the VDA cannot robustly estimate EF . However, it becomes moister on DOYs 210–259, and the EF retrievals follow the observations more closely. These results indicate that the sequences of air temperature and humidity in dry/sparsely vegetated sites do not have enough information to constrain EF .

The high soil moisture can result in negative sensible heat flux, which makes EF observations larger than one [44,110]. This occurs on DOYs 184, 201, 206, 209, and 214 in the Willow Creek; DOY 201 in the Brookings; and DOYs 206 and 242 in the Bondville. Nonetheless, in order to prevent numerical instabilities, EF estimates are set to be less than 0.99 in the VDA approach, causing the estimations to deviate from observations when they are above unity.

Table 4 shows the MAE and RMSE of the EF estimates at the six study sites. As anticipated, the MAE and RMSE of the EF estimates are lower in wet and/or densely vegetated sites compared to dry and/or slightly vegetated sites. The EF estimates have the highest MAE and RMSE of 0.152 and 0.198 at Desert (dry and barren land). The lowest MAE and RMSE values of 0.039 and 0.053 are observed at Arou (wet and dense vegetation cover).

To evaluate the performance of the VDA approach in various vegetative and climatic conditions, the scatterplot of half-hourly H and LE estimates was compared with the observations in Figures 5 and 6. As shown, the VDA approach performs better at wet/densely vegetated sites. The most and least accurate turbulent heat fluxes estimates are obtained at Arou and Desert, respectively. H and LE estimates mostly fall around the 45-degree line at Arou and Willow Creek. While at Desert, H is overestimated for H values of higher than $\sim 200 \text{ W m}^{-2}$ and LE retrievals are far from the 45-degree line. These outcomes show that the information content of the atmospheric state variables (e.g., air temperature and specific humidity) for estimating the turbulent heat fluxes significantly reduces in dry/sparsely vegetated sites (e.g., Audubon and Desert). H and LE estimates at Bondville and Brookings are comparable, and agree fairly well with the observations. Overall, the results indicate that the sequences of air temperature and specific humidity have a significant amount of information for partitioning the available energy between turbulent heat fluxes at sites with high SM and/or LAI values, but their information content significantly reduces at sites with low SM and/or LAI.

Table 4. MAE and RMSE of *EF* estimates from the VDA approach at the six study sites. Mean soil moisture ($\text{m}^3 \text{m}^{-3}$) and LAI ($\text{m}^2 \text{m}^{-2}$) over the modeling periods are also presented.

Site	<i>EF</i>		SM	LAI
	MAE	RMSE		
Arou	0.039	0.053	0.36	3.57
Willow Creek	0.067	0.079	0.22	5.67
Brookings	0.065	0.083	0.29	1.72
Bondville	0.073	0.091	0.16	2.24
Audubon	0.146	0.178	0.12	0.54
Desert	0.152	0.198	0.03	0.00

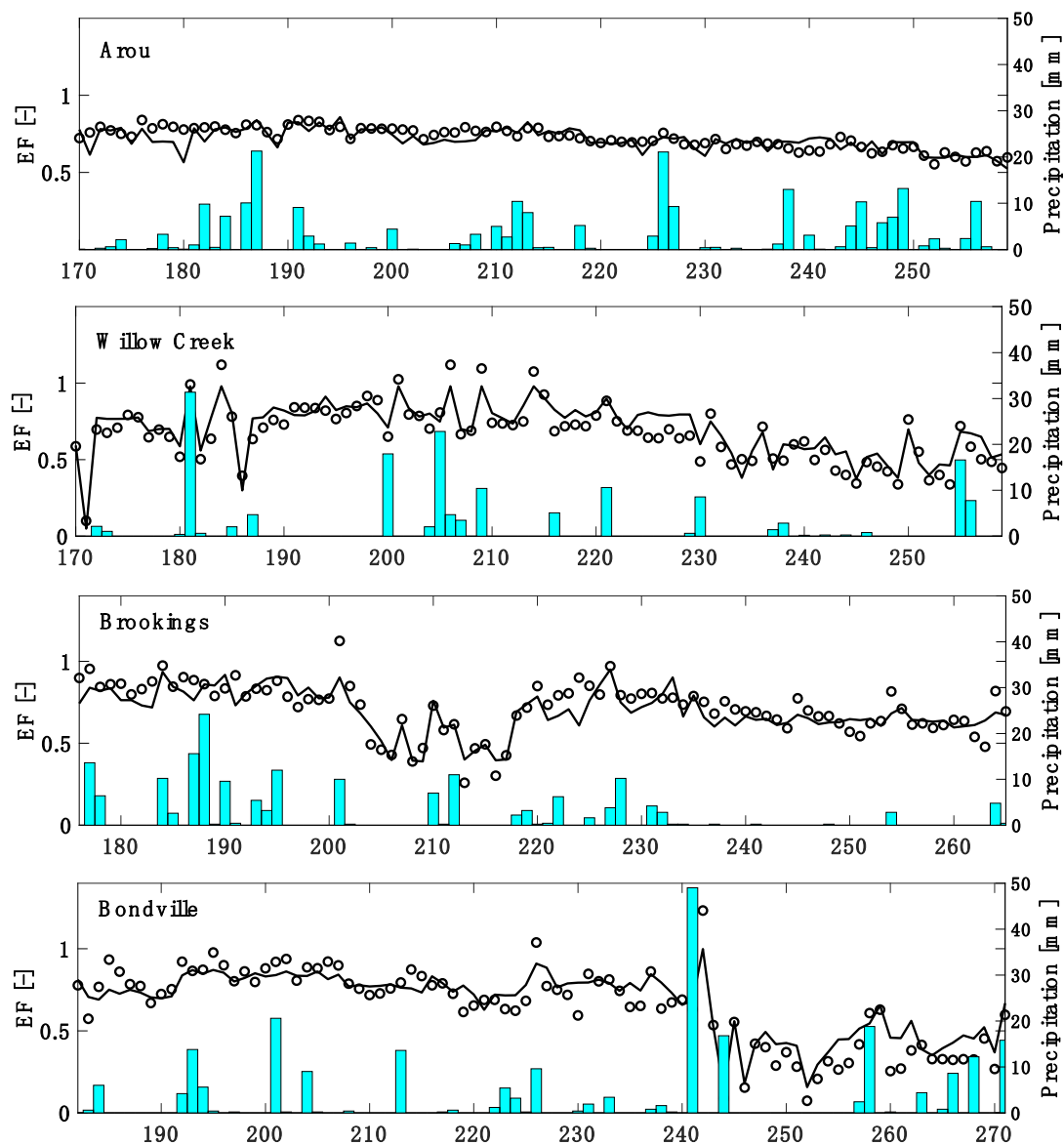


Figure 4. Cont.

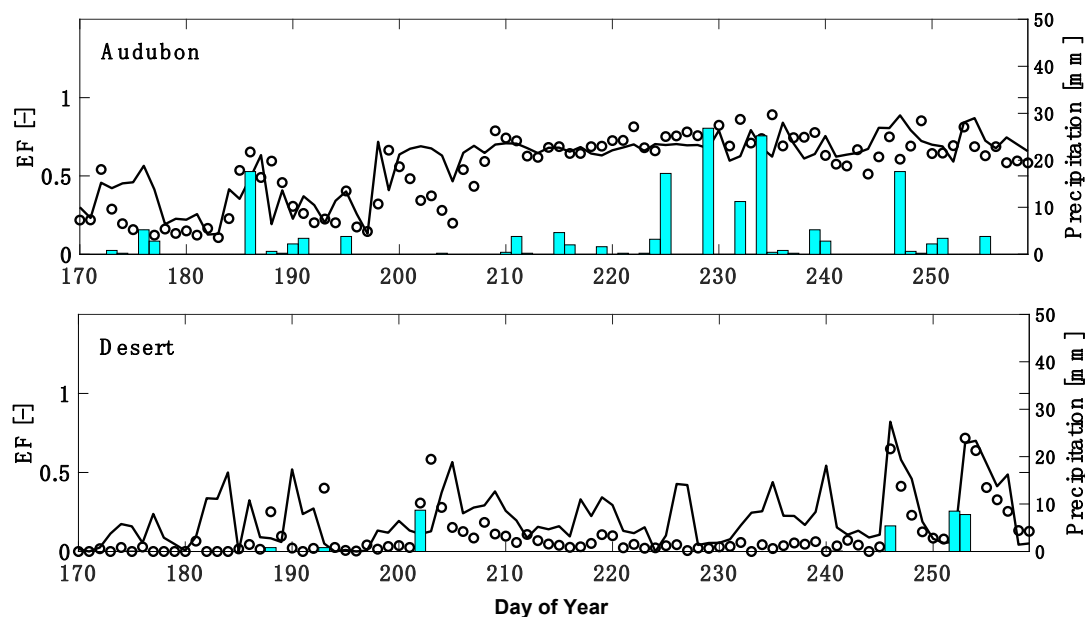


Figure 4. Time series of estimated (solid lines) and observed (open circles) EF values. Precipitations are shown by blue bars.

At all the study sites, LE estimates are more sparsely scattered around the 1:1 line compared to H estimates. This is due to the fact that errors in H estimates are due to uncertainties in C_{HN} estimates (see Equation (1)) but errors in LE retrievals stem from uncertainties in both H and EF estimates (see Equation (3)). More sources of errors increase the scattering of LE estimates [44,81,83].

The discrepancy between the EF , H , and LE estimates and corresponding observations might be due to the measurement errors and simplistic assumptions, such as the constant monthly C_{HN} , constant daily EF , insignificant advection, and convectively well mixed boundary layer, which results in constant profiles of the potential temperature and specific humidity with height.

Figure 7 compares the time series of daily H estimates from the VDA and open loop approaches with the measurements at the Arou, Willow Creek, Brookings, Bondville, Audubon, and Desert, sites. Similarly, Figure 8 compares the time series of daily LE retrievals with the observations. As expected, the VDA approach generates more accurate H and LE values at the energy-limited sites (e.g., Arou, Willow Creek, Bondville, and Brookings). At these sites, H and LE estimates can capture the day-to-day fluctuations in the observations. At the water-limited sites (e.g., Audubon and specifically Desert), VDA cannot capture the daily variations in LE . The VDA approach overestimates (underestimates) H at Desert (Audubon). In the open loop approach, air temperature and specific humidity measurements are not assimilated into the VDA approach, and thus the initial guesses for C_{HN} and EF are not updated. In this approach, the ABL potential temperature (θ) and specific humidity (q) are estimated by integrating Equations (4) and (5) forward in time using the initial guesses of C_{HN} and EF . The large discrepancy between the turbulent heat fluxes estimates from VDA and the open loop at the wet and/or highly vegetated sites shows that the performance of VDA significantly improves at these sites by using the information content of atmospheric state variables.

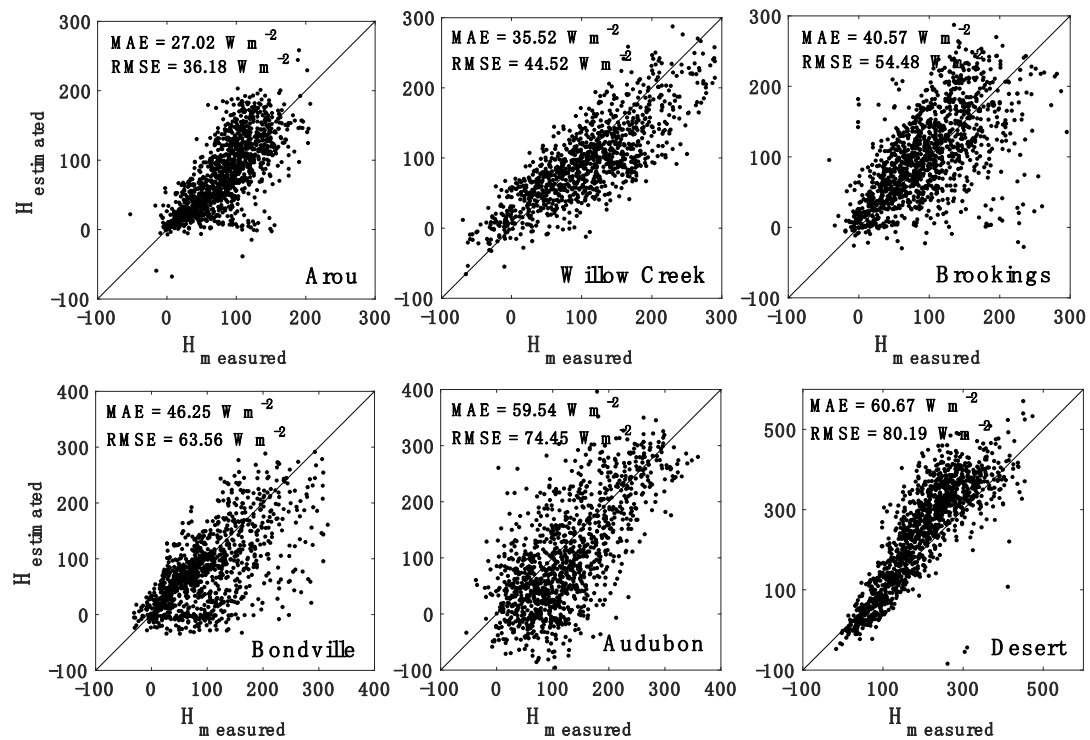


Figure 5. Scatterplot of half-hourly sensible heat flux (H) estimates versus observations at the six investigated sites.

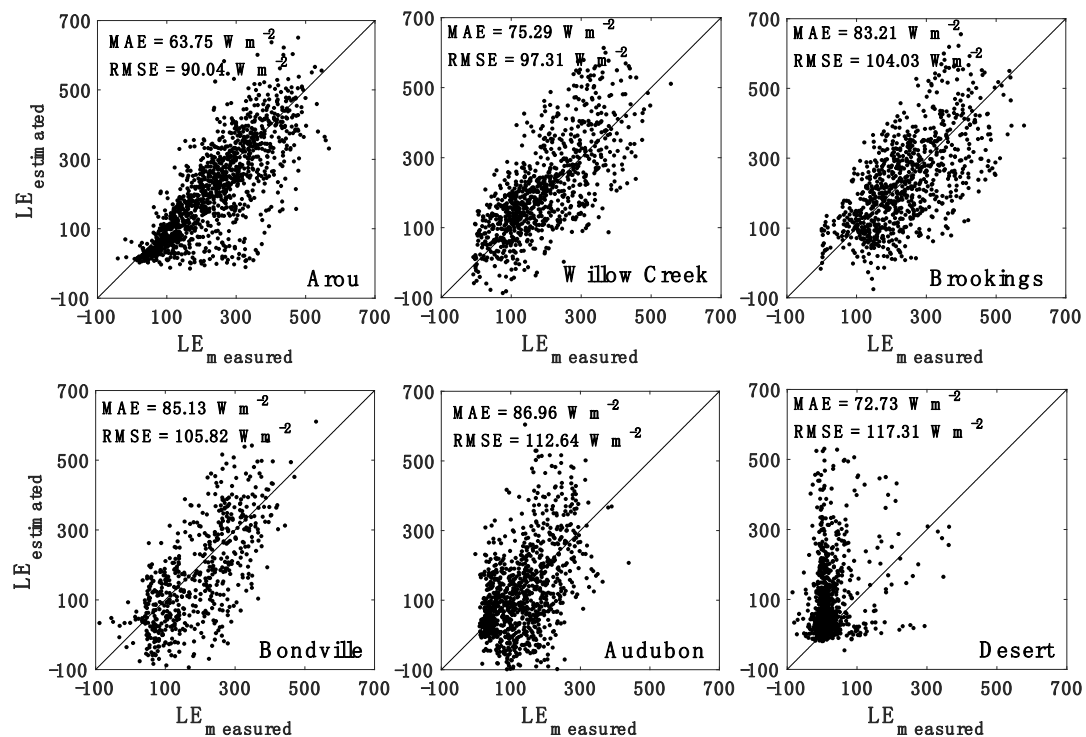


Figure 6. Scatterplot of half-hourly latent heat flux (LE) estimates versus observations at the six investigated sites.

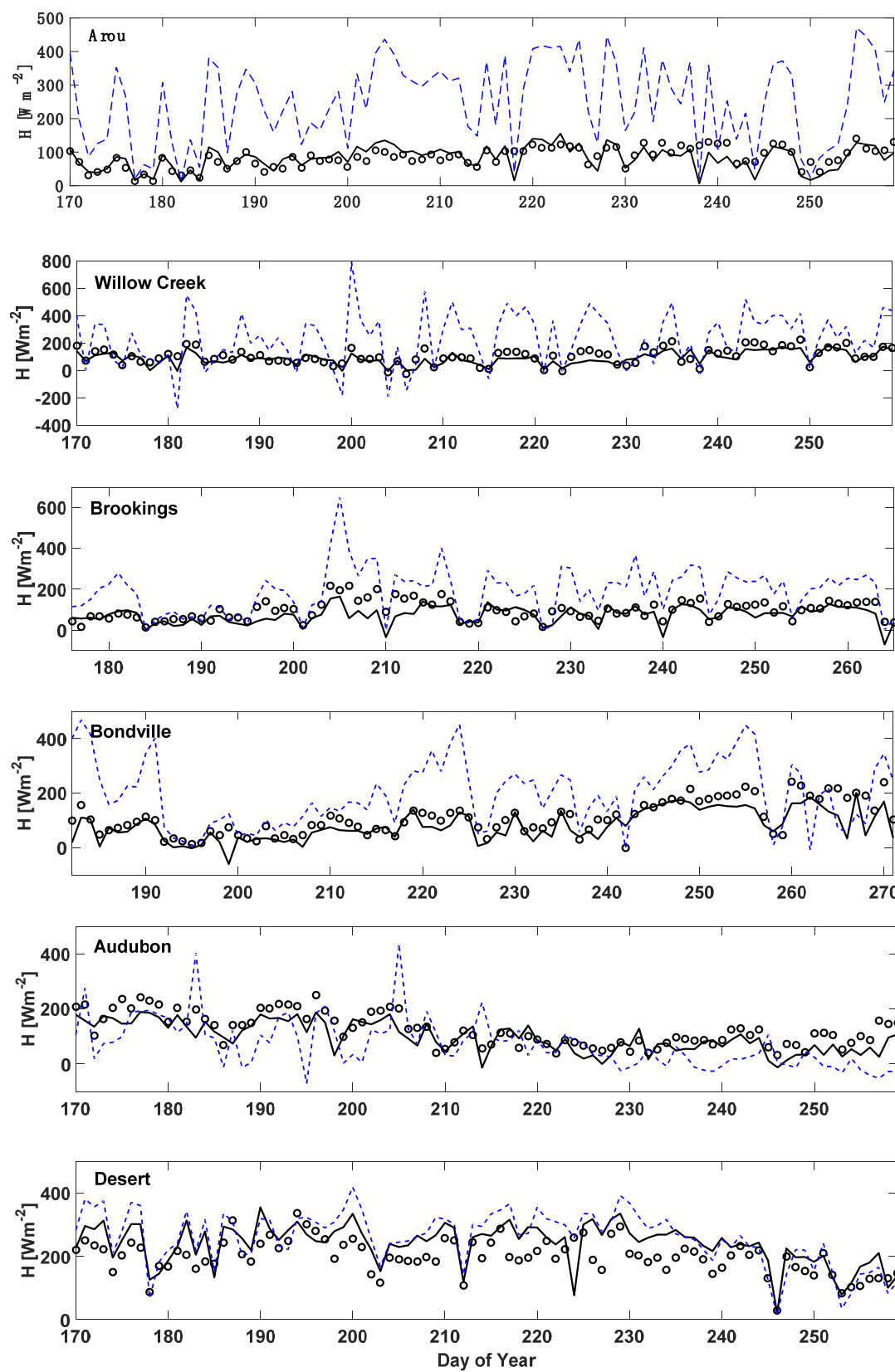


Figure 7. Time series of sensible heat flux (H) estimates from the VDA (solid lines) and open loop (blue dashed lines) approaches at the six study sites. Observed H values are shown by open circles.

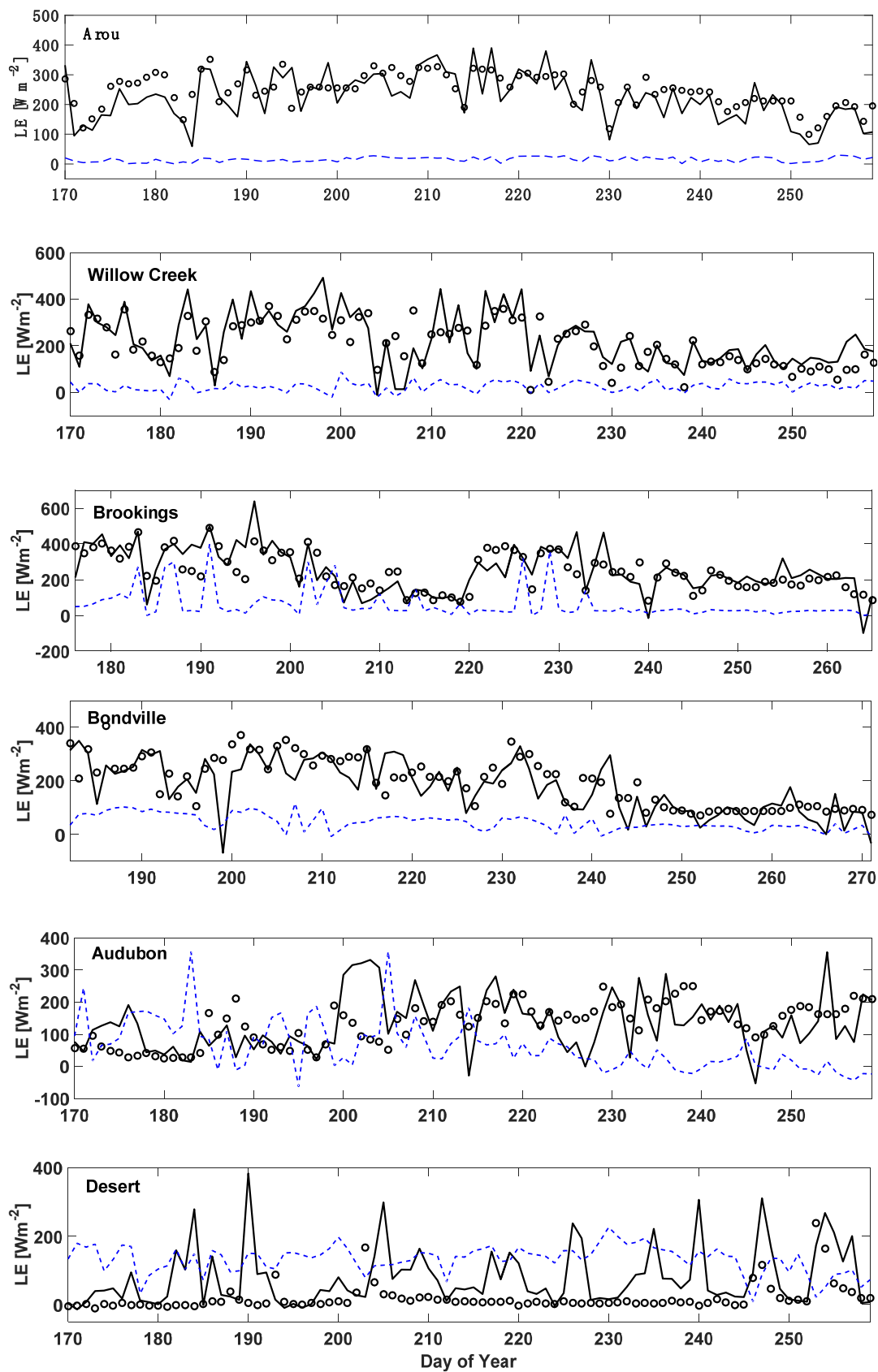


Figure 8. Time series of latent heat flux (LE) estimates from the VDA (solid lines) and open loop (blue dashed lines) approaches at the six study sites. Observed LE values are shown by open circles.

The MAE and RMSE of half-hourly sensible and latent heat fluxes estimates from the VDA and open loop approaches at the six study sites are shown in Table 5. Similarly, Table 6 indicates the MAE and RMSE of daily H and LE retrievals. The high MAE and RMSE of turbulent heat fluxes estimates from VDA at the Desert and Audubon sites are attributed to their dry land and/or sparse vegetation. Compared to Desert and Audubon, Arou, Brookings, Bonville, and Willow Creek are wetter and have denser vegetation cover. Hence, the errors of VDA H and LE retrievals at Arou, Brookings, Bonville, and Willow Creek are lower than those of Desert and Audubon. Arou has the lowest MAE and RMSE values because it has a dense vegetation cover and the highest soil moisture.

Table 5. MAE and RMSE of half-hourly H and LE estimates from the VDA and open loop approaches at the six experimental sites.

Site	Method	H (Wm^{-2})		LE (Wm^{-2})	
		MAE	RMSE	MAE	RMSE
Arou	VDA (Open-loop)	27.02 (205.92)	36.18 (242.09)	63.75 (219.33)	90.04 (247.15)
Willow Creek	VDA (Open-loop)	35.52 (188.52)	44.52 (223.67)	75.29 (179.98)	97.31 (239.42)
Brookings	VDA (Open-loop)	40.57 (105.89)	54.48 (138.58)	83.21 (212.36)	104.03 (239.00)
Bondville	VDA (Open-loop)	46.25 (118.67)	63.56 (158.02)	85.13 (156.58)	105.82 (188.92)
Audubon	VDA (Open-loop)	59.54 (107.75)	74.45 (127.97)	86.96 (140.09)	112.64 (166.11)
Desert	VDA (Open-loop)	60.67 (77.78)	80.19 (103.76)	72.73 (95.96)	117.31 (156.28)
Six-site average	VDA (Open-loop)	44.93 (134.09)	58.89 (165.68)	77.85 (167.38)	104.53 (206.15)

Table 6. MAE and RMSE of daily H and LE estimates from the VDA and open loop approaches at the six experimental sites.

Site	Method	H (Wm^{-2})		LE (Wm^{-2})	
		MAE	RMSE	MAE	RMSE
Arou	VDA (Open-loop)	18.07 (172.66)	25.43 (197.61)	43.99 (231.71)	55.81 (237.78)
Willow Creek	VDA (Open-loop)	30.05 (157.65)	37.03 (197.65)	56.93 (179.33)	74.46 (200.28)
Brookings	VDA (Open-loop)	32.05 (100.47)	45.01 (123.03)	57.79 (185.88)	82.28 (207.54)
Bondville	VDA (Open-loop)	31.97 (108.15)	45.21 (134.12)	55.34 (152.44)	77.88 (172.74)
Audubon	VDA (Open-loop)	46.16 (74.73)	58.13 (91.77)	71.77 (125.67)	89.57 (145.45)
Desert	VDA (Open-loop)	50.08 (67.07)	60.00 (80.95)	68.74 (90.23)	102.21 (132.62)
Six-site average	VDA (Open-loop)	34.73 (113.46)	45.14 (137.52)	59.09 (160.88)	80.37 (182.74)

In both Tables 5 and 6, the lower MAE and RMSE values from VDA imply that the assimilation of reference-level air temperature and humidity improve the open loop H and LE estimates. The six-site average MAE and RMSE of daily H estimate from VDA (open loop) are 34.73 Wm^{-2} (113.46 Wm^{-2}) and 45.14 Wm^{-2} (137.52 Wm^{-2}), respectively. The corresponding MAE and RMSE values for daily LE estimates are 59.09 Wm^{-2} (160.88 Wm^{-2}) and 80.37 Wm^{-2} (182.74 Wm^{-2}), respectively. By assimilating T_a and q_a , on average, the MAE and RMSE of the daily H (LE) estimates from VDA are reduced by 69.4% (63.3%) and 67.2% (56%) compared to those of the open loop. By the assimilation of air temperature and specific humidity, the MAE and RMSE of the daily H (LE) estimates from the open loop is reduced by 89.5% (81%) and 87.1% (76.5%) at Arou, and 80.9% (68.3%) and 81.3% (62.8%) at Willow Creek. The corresponding values at Desert and Audubon are 25.3% (23.8%) and 25.9% (22.9%), and 38.2% (42.9%) and 36.7% (38.4%), respectively. These results show that the assimilation of T_a and q_a leads to a higher improvement in the H and LE estimates at wet/densely vegetated sites.

The VDA approach iteratively improves the C_{HN} and EF estimates by minimizing the difference between the ABL potential temperature and specific humidity estimates from Equations (4) and (5) (i.e., θ and q), and the corresponding values obtained from the reference-level air temperature and specific humidity via the MOST (i.e., θ_{SL} and q_{SL}) (Appendix B). Thus, a close agreement between the θ and θ_{SL} , and q and q_{SL} (e.g., Arou) shows that the VDA approach can successfully update the initial guesses of C_{HN} and EF and converges to their optimal values. On the other hand, a significant misfit between the θ_{SL} and θ , and q_{SL} and q (e.g., Desert) implies that the VDA cannot effectively improve the initial guesses of C_{HN} and EF and converges to the inaccurate C_{HN} and EF values. Figure 9 shows half-hourly θ estimates from VDA versus θ_{SL} values. Similarly, Figure 10 indicates half-hourly q estimates versus

q_{SL} values. As shown, at Arou and Willow Creek, the θ and q estimates from VDA agree well with θ_{SL} and q_{SL} , respectively. This shows that in wet and/or densely vegetated sites, the VDA approach can take advantage of the significant amount of information in the sequences of air temperature and humidity to optimize C_{HN} and EF , and consequently minimize the difference between θ and θ_{SL} , and q and q_{SL} . At the Brookings and Bondville sites, the θ and q estimates are in fairly good agreement with θ_{SL} and q_{SL} , respectively, implying that the time series of the atmospheric state variable have some information to constrain C_{HN} and EF , and retrieve turbulent heat fluxes. At the Desert and Audubon sites, θ and q estimates are more scattered around the 1:1 line, showing the lack of sufficient information in the sequence of air temperature and humidity to accurately tune C_{HN} and EF .

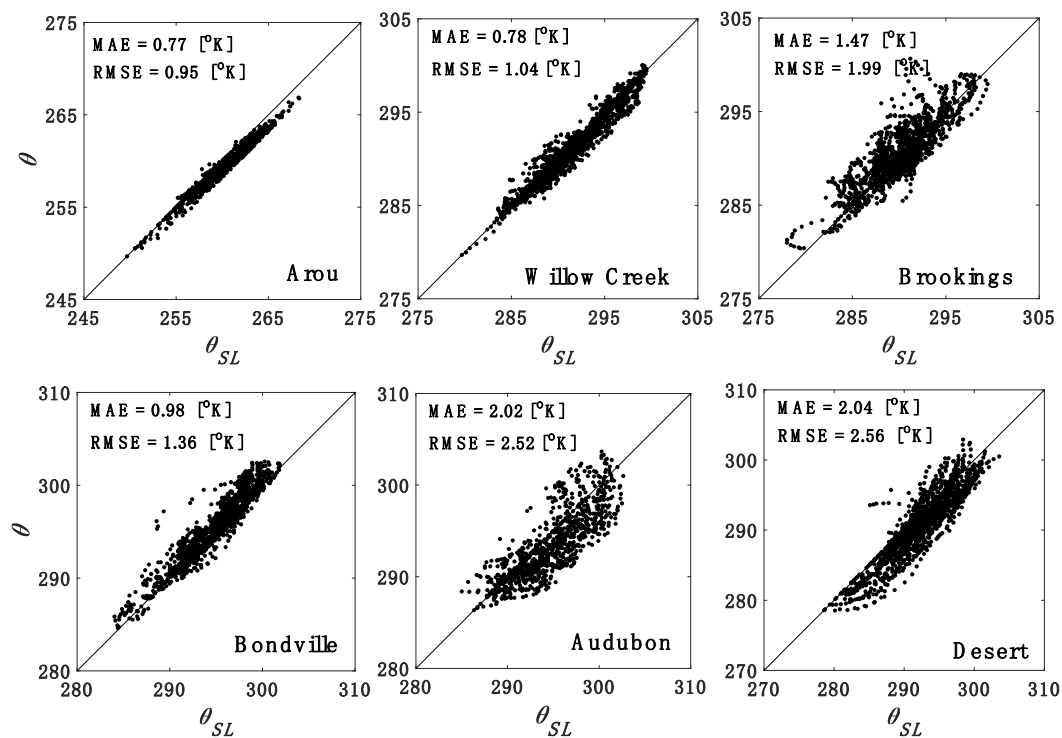


Figure 9. Scatterplot of half-hourly potential temperature (θ) estimates from VDA versus θ_{SL} at the six experimental sites.

The RMSE of the θ (q) estimates at the Desert, Audubon, Bondville, Brookings, Willow Creek, and Arou sites are 2.56 K (0.0021 kg kg⁻¹), 2.52 K (0.0015 kg kg⁻¹), 1.36 K (0.0012 kg kg⁻¹), 1.99 K (0.0012 kg kg⁻¹), 1.04 K (0.0011 kg kg⁻¹), and 0.95 K (0.0009 kg kg⁻¹), respectively. As anticipated, the RMSEs of the θ and q estimates decrease as LAI and/or SM increase. Arou (with the highest SM) has the lowest RMSEs for θ and q . In contrast, Desert (with the lowest LAI and SM) has the highest RMSEs. As mentioned earlier, in dry sites (e.g., Desert and Audubon), evaporation is mainly controlled by the land surface state variable (i.e., LST). Hence, assimilating sequences of air temperature and specific humidity cannot robustly constrain C_{HN} and EF , leading to larger errors in the θ and q estimates. Bondville and Brookings are neither as sparsely vegetated as Desert and Audubon nor as densely vegetated as Willow Creek and Arou. The RMSEs of the θ and q estimates at these sites are smaller than those of Desert and Audubon but larger than those of Willow Creek and Arou.

Figure 11 indicates the mean diurnal cycles of the measured and estimated H and LE over the whole modeling period for the six study sites. As anticipated, the magnitude and phase of the diurnal cycles of retrieved sensible and latent heat fluxes from VDA agree well with those of the observations at the Arou and Willow Creek sites. For Audubon and especially Desert, there is a large discrepancy between the diurnal cycles of the estimated and observed H and LE , showing that the performance of the VDA approach significantly degrades in dry and/or sparsely vegetated sites. The results for the

Bondville and Brookings sites show that assimilating the state variables of the atmosphere (i.e., θ and q) can capture the diurnal cycles of H and LE relatively well.

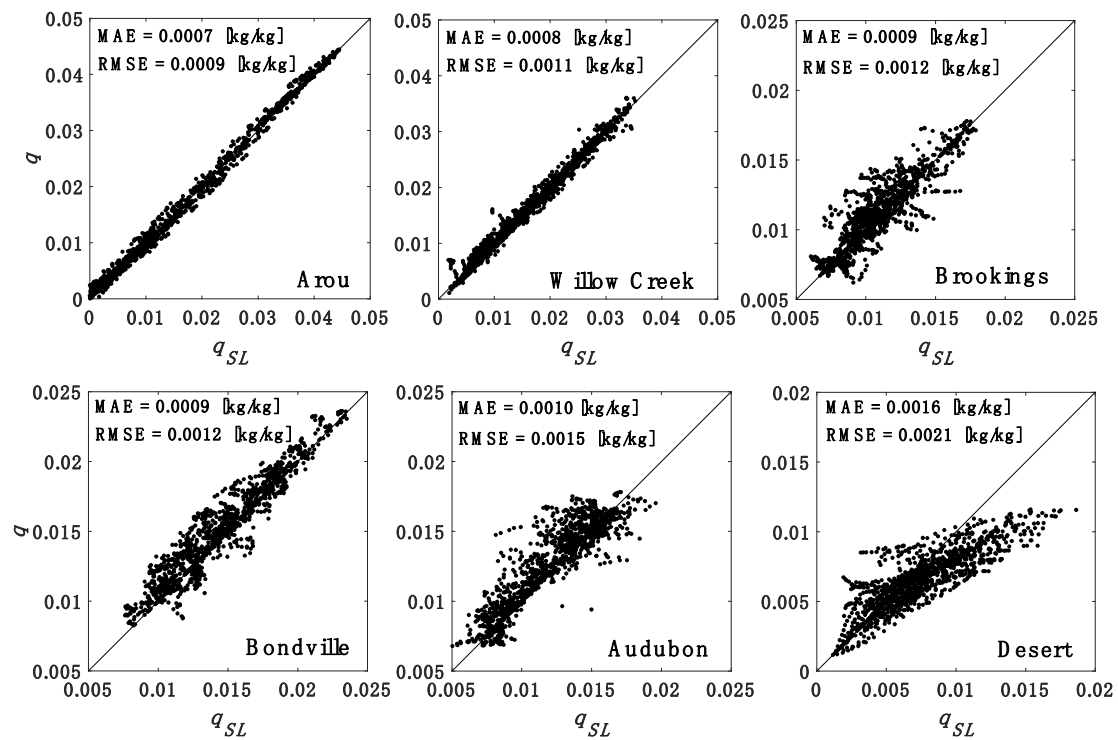


Figure 10. Scatterplot of half-hourly specific humidity (q) estimates versus q_{SL} at the six experimental sites.

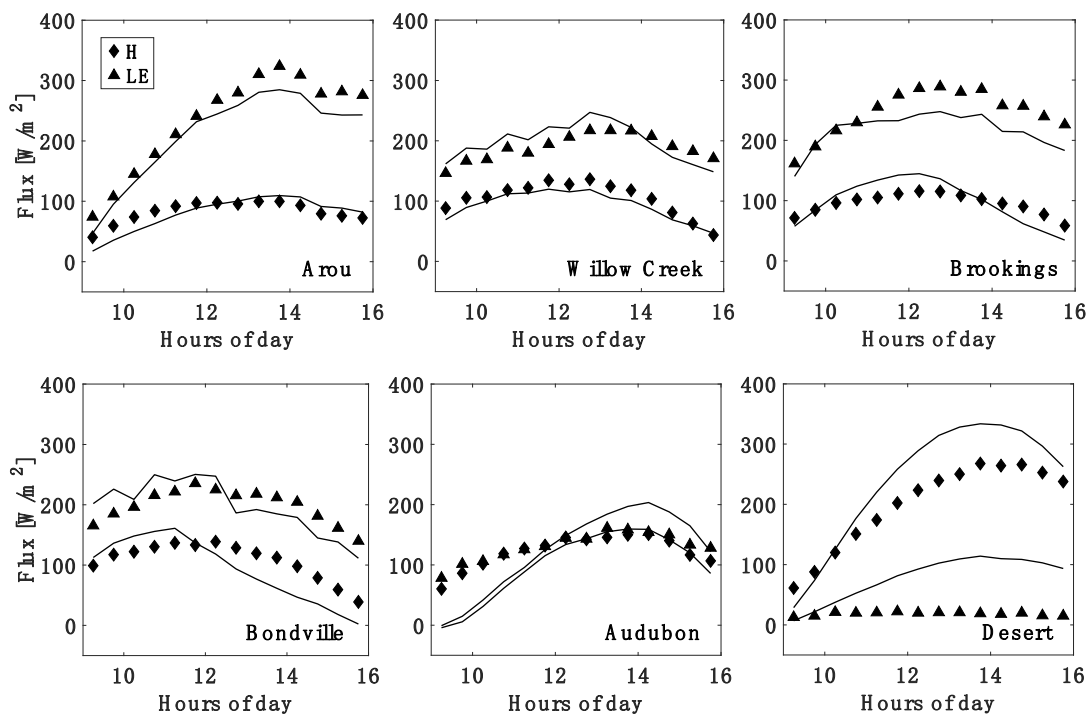


Figure 11. Mean diurnal cycle of estimated (solid lines) and measured (symbols) turbulent heat fluxes from the VDA approach for the six study sites.

5. Conclusions

In this study, sequences of reference-level air temperature and humidity were assimilated into a VDA approach to partition the available energy between the sensible (H) and latent (LE) heat fluxes at six sites (namely, Arou, Audubon, Bondville, Brookings, Desert, and Willow Creek) with different vegetative and climatic conditions. The VDA approach takes advantage of the implicit information in the time series of reference-level air temperature and specific humidity (as the state variables of the atmosphere) to estimate the neutral bulk heat transfer coefficient, C_{HN} (that scales the sum of H and LE), and evaporative fraction, EF (that represents the partitioning between H and LE).

The sites with higher leaf area index (LAI) values showed larger C_{HN} estimates. Additionally, at wet and/or densely vegetated sites, the variations in C_{HN} estimates were consistent with those of LAI. This consistency weakened in dry and/or sparsely vegetated sites. Similarly, the EF estimates agreed well with the observations in terms of the magnitude and day-to-day dynamics in wet and/or densely vegetated sites (e.g., Arou and Willow Creek), but this agreement degraded in dry and/or sparsely vegetated sites (e.g., Desert and Audubon). The RMSE of EF estimates at Desert (dry barren land) was 0.198, which is 73.2% higher than that of 0.053 at Arou (wet grassland). These results show that the sequences of air temperature and specific humidity have a significant amount of information on the partitioning of available energy between H and LE in wet and/or densely vegetated sites. This information content decreases by the reduction of soil moisture and/or LAI.

The RMSEs of daily sensible (latent) heat flux estimates at the Arou, Willow Creek, Brookings, Bondville, Desert, and Audubon sites were 25.43 W m⁻² (55.81 W m⁻²), 37.03 W m⁻² (74.46 W m⁻²), 45.01 W m⁻² (82.28 W m⁻²), 45.21 W m⁻² (77.88 W m⁻²), 58.13 W m⁻² (89.57 W m⁻²), and 60.00 W m⁻² (102.21 W m⁻²), respectively. The RMSEs of the daily H and LE estimates increased as the site became drier and/or sparser in vegetation density. This is due to the fact that in dry and/or sparsely vegetated sites (e.g., Desert and Audubon), evapotranspiration is mainly controlled by the land surface state variable (i.e., land surface temperature) rather than the atmospheric state variables (i.e., reference-level air temperature and specific humidity). Hence, the coupling between EF and the atmospheric state variables weakens and the estimation of EF from the sequences of air temperature and specific humidity becomes uncertain. In contrast, at wet and/or densely vegetated sites (e.g., Arou and Willow Creek), the evaporative demand is primarily controlled by atmospheric state variables and the VDA system can extract that information to estimate H and LE .

The RMSEs of the atmospheric boundary layer (ABL) potential temperature (θ) estimates at the Desert, Audubon, Bondville, Brookings, Willow Creek and Arou sites were 2.56, 2.52, 1.36, 1.99, 1.04, and 0.95 K, respectively. The corresponding RMSEs for the ABL humidity (q) estimates were 0.0021, 0.0015, 0.0012, 0.0012, 0.0011, and 0.0009 kg kg⁻¹. The low RMSEs of the θ and q estimates at wet and/or densely vegetated sites (e.g., Arou and Willow Creek) indicated that the VDA approach can effectively update the two key unknowns (i.e., C_{HN} and EF) and obtain their optimal values. In contrast, at dry and/or sparsely vegetated sites (e.g., Desert and Audubon), the VDA system cannot effectively update C_{HN} and EF , leading to high RMSEs for θ and q . The highest and lowest RMSEs of θ and q estimates occurred at Desert and Arou, respectively. The RMSEs of θ and q estimates at the Bondville and Brookings sites fell within those of dry/sparsely vegetated and wet/densely vegetated sites.

The magnitude and phase of the diurnal cycles of the retrieved sensible and latent heat fluxes agreed well with the observations at wet/densely vegetated sites (e.g., Arou and Willow Creek). In contrast, for the dry/lightly vegetated sites (Audubon and especially Desert), a significant difference was found between the diurnal cycles of the retrieved and observed H and LE .

Future studies should focus on the synergistic assimilation of the LST (as the state variable of land surface) and the reference-level air temperature and specific humidity (as the state variables of atmosphere) to improve the turbulent heat flux estimates at the dry and/or sparsely vegetated sites. In addition, future studies should be advanced by taking C_{HN} as a function of LAI.

Author Contributions: Conceptualization, E.T. and S.M.B.; methodology, E.T. and S.M.B.; software, E.T., S.M.B. and T.X.; validation, E.T. and S.M.B.; data curation, E.T. and T.X.; writing—original draft preparation, E.T.; writing—review and editing, S.M.B., E.H.; visualization, E.T.; supervision, S.M.B.; project administration, S.M.B.; funding acquisition, S.M.B. All authors have read and agreed to the published version of the manuscript.

Funding: This research was funded by the United State Geological Service (USGS) grant, G16AP00049 (2018AS485BB) and United State Department of Agriculture (USDA) grant 69-3A75-17-54 to the University of Hawaii at Manoa.

Acknowledgments: It is a contributed paper of the Water Resources Research Center, University of Hawaii at Manoa, Honolulu, Hawaii.

Conflicts of Interest: The authors declare no conflict of interest.

Appendix A. List of symbols

B	Stanton number	[-]
B_{EF}^{-1}	inverse background error covariance of EF	[-]
B_R^{-1}	inverse background error covariance of R	[-]
C_{HN}	neutral bulk heat transfer coefficient	[-]
c_p	specific heat capacity of dry air	[J kg ⁻¹ K ⁻¹]
D_1, D_2	dissipation of mechanical turbulent energy	[m ³ s ⁻³]
d	zero-plane displacement height	[m]
E	evaporative rate from ground	[kg m ⁻² s ⁻¹]
EF	evaporative fraction	[-]
f	atmospheric stability correction function	[-]
G	ground heat flux	[W m ⁻²]
G_*	production of mechanical turbulent energy	[m ³ s ⁻³]
g	gravitational acceleration	[m s ⁻²]
H	sensible heat flux	[W m ⁻²]
H_{top}	entrainment sensible heat flux	[W m ⁻²]
H_v	virtual heat flux	[W m ⁻²]
h	mixed-layer height	[m]
J	objective functional	[-]
k	von Karman's constant	[-]
κ	empirical constant	[kg m ⁻²] ^{-1/7}
L	Monin-Obhukov length	[m]
L_v	latent heat of vaporization	[J kg ⁻¹]
LE	latent heat flux	[W m ⁻²]
LE_{top}	entrainment latent heat flux	[W m ⁻²]
LAI	leaf area index	[m ² m ⁻²]
m	constant	[-]
N	number of days in the assimilation period	
P_h	pressure at height h	[Pa]
P_s	surface pressure	[Pa]
q	mixed layer specific humidity (equation 5b)	[kg kg ⁻¹]
q_a	specific humidity at the reference-level	[kg kg ⁻¹]
q_h	specific humidity immediately above mixed layer	[kg kg ⁻¹]
q_{SL}	specific humidity at the bottom of mixed layer (equation B2)	[kg kg ⁻¹]
R	transformation variable	[-]
R_{Ad}	downwelling longwave radiation from within the mixed layer	[W m ⁻²]
R_{Au}	upwelling longwave radiation from within the mixed layer	[W m ⁻²]
R_{ad}	downwelling longwave radiation from above the mixed layer	[W m ⁻²]
R_d	gas constant for dry air	[J kg K ⁻¹]
R_{gu}	upwelling longwave radiation from ground into the mixed layer	[W m ⁻²]

Ri	Richardson number	[-]
R_n	net radiation at the surface	[W m ⁻²]
R_s^\downarrow	incoming solar radiation	[W m ⁻²]
R_v	gas constant for water vapor	[J kg K ⁻¹]
R_q^{-1}	inverse error covariance of q	[-]
R_θ^{-1}	inverse error covariance of θ	[K ⁻²]
SL	surface layer	[-]
T	land surface temperature	[K]
T_a	reference-level air temperature	[K]
T_h	air temperature immediately above the mixed layer	[K]
t	time	[s]
U	wind speed at the reference-level	[m s ⁻¹]
u_{SL}	wind speed at the top of the surface layer	[m s ⁻¹]
u_*	friction velocity	[m s ⁻¹]
z_{0h}	roughness length scales for heat	[m]
z_{0m}	roughness length scales for momentum	[m]
z_{SL}	surface-layer height	[m]
z_{ref}	reference-level height	[m]
z_{veg}	vegetation height	[m]
α	surface albedo	[-]
δ_q	specific humidity inversion strength	[kg kg ⁻¹]
δ_θ	potential temperature inversion strength	[K]
ε_a	atmospheric emissivity	[-]
ε_{ad}	effective emissivity above the mixed-layer	[-]
ε_d	effective mixed-layer downward emissivity	[-]
ε_u	effective mixed-layer upward emissivity	[-]
ε_m	mixed-layer bulk emissivity	[-]
ε_s	surface emissivity	[-]
γ_q	lapse rate of q above the mixed layer	[kg kg ⁻¹ m ⁻¹]
γ_θ	lapse rate of θ above the mixed layer	[K m ⁻¹]
λ_1, λ_2	lagrange multipliers	[-]
Ψ_h	stability function for heat	[-]
Ψ_m	stability function for momentum	[-]
Ψ_q	stability function for water vapor	[-]
ρ	air density	[kg m ⁻³]
σ	Stefan-Boltzmann constant	[W m ⁻² K ⁻⁴]
θ	Mixed layer potential temperature (equation 5a)	[K]
θ_a	reference-level potential temperature	[K]
θ_{SL}	potential temperature at the bottom of mixed layer (equation B1)	[K]
φ	mechanical turbulence dissipation parameter	[-]
ξ	stability parameter	[-]

Appendix B. Monin–Obukhov Similarity Theory (MOST)

The potential temperature, specific humidity, and wind speed at the top of the surface layer (i.e., θ_{SL} , q_{SL} , and u_{SL}) are found by expanding θ_a , q_a , and U from the reference height (z_{ref}) to the bottom of the mixed layer (z_{SL}) via the Monin–Obukhov similarity theory (MOST) [77]:

$$\theta_{SL} = \theta_a - \frac{H}{ku_*\rho c_p} \left[\ln\left(\frac{z_{SL} - d}{z_{ref} - d}\right) - \Psi_h\left(\frac{z_{SL} - d}{L}\right) + \Psi_h\left(\frac{z_{ref} - d}{L}\right) \right], \quad (A1)$$

$$q_{SL} = q_a - \frac{LE}{ku_*\rho L_v} \left[\ln\left(\frac{z_{SL} - d}{z_{ref} - d}\right) - \Psi_q\left(\frac{z_{SL} - d}{L}\right) + \Psi_q\left(\frac{z_{ref} - d}{L}\right) \right], \quad (A2)$$

$$u_{SL} = U + \frac{u_*}{k} \left[\ln \left(\frac{z_{SL} - d}{z_{ref} - d} \right) - \Psi_m \left(\frac{z_{SL} - d}{L} \right) + \Psi_m \left(\frac{z_{ref} - d}{L} \right) \right], \quad (A3)$$

where k is the von Karman's constant; d is zero-plane displacement height (d is 2/3 of the vegetation height, z_{veg}); L_v is the latent heat of vaporization; and Ψ_h , Ψ_m , and Ψ_q are the stability functions for heat, momentum, and water vapor and are given by [77,111,112]:

$$\Psi_h(\xi) = \Psi_q(\xi) = \begin{cases} 2 \ln \left[\frac{(1 + \sqrt{1 - 16\xi})}{2} \right] & \xi < 0 \\ -5\xi & 0 \ll \xi \ll 1 \\ -5 - 5 \ln(\xi) & \xi > 1 \end{cases} \quad (A4)$$

$$\Psi_m(\xi) = \begin{cases} 2 \ln \left(\frac{1 + (1 - 16\xi)^{\frac{1}{4}}}{2} \right) + \ln \left(\frac{1 + \sqrt{1 - 16\xi}}{2} \right) - 2 \tan^{-1} (1 - 16\xi)^{\frac{1}{4}} + \frac{\pi}{2} & \xi < 0 \\ -5\xi & 0 \ll \xi \ll 1 \\ -5 - 5 \ln(\xi) & \xi > 1 \end{cases} \quad (A5)$$

where ξ is the stability parameter, which is defined as the ratio of the measurement height to the Monin–Obukhov length (z_{ref}/L) [77,93]. The Monin–Obukhov length is defined as:

$$L = \frac{-\rho c_p \theta_a \left(1 + \frac{R_d}{R_v} q_a \right) u_*^3}{kgH}, \quad (A6)$$

where R_d is the gas constant for dry air ($287 \text{ J kg}^{-1} \text{ } ^\circ\text{C}^{-1}$), R_v is the gas constant for water vapor ($461 \text{ J kg}^{-1} \text{ } ^\circ\text{C}^{-1}$), g is the gravitational acceleration, ρ is the air density, and c_p is the specific heat capacity of air. Sensible (H) and latent heat fluxes (LE) are obtained respectively from Equations (1) and (3). u_* is the friction velocity that is related to the wind speed measurements at the reference level (U) via [77]:

$$u_* = \frac{kU}{\ln \left(\frac{z_{ref} - d}{z_{0m}} \right) - \Psi_m \left(\frac{z_{ref} - d}{L} \right) + \Psi_m \left(\frac{z_{0m}}{L} \right)}, \quad (A7)$$

where z_{0m} is the momentum roughness height. The neutral bulk heat transfer coefficient for heat (C_{HN}) can be related to the roughness length scales for heat (z_{0h}) and momentum (z_{0m}) via [50]:

$$C_{HN} = \frac{k^2}{\ln^2 \left(\frac{z_{ref}}{z_{0h}} \right) - kB^{-1} \ln \left(\frac{z_{ref}}{z_{0h}} \right)}, \quad (A8)$$

where z_{0h} is the roughness length for heat. The roughness length scales for heat and momentum are related through [50,111,112]:

$$kB^{-1} = \ln \left(\frac{z_{0m}}{z_{0h}} \right), \quad (A9)$$

where B is the Stanton number. Rigden and Salvucci [77] related kB^{-1} to the vegetation height (z_{veg}) through:

$$B^{-1} = \begin{cases} 2 & \text{low } z_{veg} \\ 5 & \text{intermediate } z_{veg} \\ 8 & \text{tall } z_{veg} \end{cases}. \quad (A10)$$

The following steps explain how θ_{SL} and q_{SL} are obtained from θ_a and q_a :

1. Guess a reasonable value for u_* .
2. Substitute u_* from step 1 in B6 to estimate L .
3. Estimate kB^{-1} from B10.

4. Substitute the C_{HN} estimate from the VDA approach and obtained kB^{-1} from step 3 in B8 to find z_{0h} .
5. Substitute z_{0h} from step 4 in B9 to find z_{0m} .
6. Substitute z_{0m} from step 5 and L from step 2 in B7 to find u_* .
7. Repeat steps 2–6 until the algorithm converges (i.e., the difference between u_* estimates from the last two iterations becomes smaller than 0.01 m/s). This step gives us u_* , z_{0h} , z_{0m} , and L estimates for a given C_{HN} value.
8. Substitute u_* and L from step 7 in B1 and B2 to estimate θ_{SL} and q_{SL} .

As the potential temperature and specific humidity are invariant through the mixed layer, $\theta(t = t_0) = \theta_{SL}(t = t_0)$, and $q(t = t_0) = q_{SL}(t = t_0)$, which give us the initial conditions for Equations (4) and (5). The estimated u_{SL} is used to integrate Equation (10) forward in time and the estimated θ_{SL} and q_{SL} are utilized to integrate Equations (A11) and (A13) backward in time.

Appendix C. Euler–Lagrange Equations

The VDA approach uses the initial guesses for EF and R as well as the initial conditions $\theta(t = t_0)$ and $q(t = t_0)$ to integrate the ABL potential temperature and specific humidity (i.e., Equations (4) and (5) forward in time. Then, Equations (A11) and (A13) are integrated backward in time using the final conditions Equations (A12) and (A14), respectively. Finally, the model updates the parameters EF and R using Equations (A15) and (A16), respectively. These steps are repeated until convergence is reached:

$$\begin{aligned} \frac{d\lambda_1}{dt} = \frac{1}{h} & \left[\frac{2R_{\theta}^{-1}(\theta - \theta_{SL})}{\rho c_p} \right. \\ & + \lambda_1 \left[-\frac{4\theta G_* e^{-\varphi h}}{gh\delta_{\theta}} - \frac{0.2f(Ri)U(T-T_a)e^R}{\delta_{\theta}} \left(1 + \frac{0.07EF}{1-EF}\right) \right. \\ & + \frac{0.2\theta e^R f(Ri)U}{\delta_{\theta}} \left(1 + \frac{0.07EF}{1-EF}\right) \left(\frac{P_s}{P_h}\right)^{\frac{R_d}{c_p}} \\ & - \frac{\varepsilon_m \varepsilon_{ad} \sigma (4\theta^3 + 12\theta^2 \delta_{\theta} + 4\delta_{\theta}^3 + 12\theta \delta_{\theta}^2)}{\rho c_p} \left(\frac{P_h}{P_s}\right)^{\frac{4R_d}{c_p}} + \frac{4\varepsilon_h \sigma \theta^3}{\rho c_p} - \frac{4\varepsilon_d \sigma \theta^3}{\rho c_p} \\ & \left. \left. + 1.32e^R f(Ri)U \left(\frac{P_s}{P_h}\right)^{\frac{R_d}{c_p}} \right] \right. \\ & + \lambda_2 \left[-\frac{2q}{c_p} \frac{G_* e^{-\varphi h}}{gh\delta_{\theta}} + \frac{0.2qe^R f(Ri)U}{c_p \delta_{\theta}} \left(\frac{P_s}{P_h}\right)^{\frac{R_d}{c_p}} \left(1 + \frac{0.07EF}{1-EF}\right) + \frac{EF e^R f(Ri)U}{(1-EF)L_v} \left(\frac{P_s}{P_h}\right)^{\frac{R_d}{c_p}} \right. \\ & \left. \left. - \frac{\delta_q}{c_p} \frac{2G_* e^{-\varphi h}}{gh\delta_{\theta}} + \frac{0.2\delta_q}{c_p \delta_{\theta}} e^R f(Ri)U \left(\frac{P_s}{P_h}\right)^{\frac{R_d}{c_p}} \left(1 + \frac{0.07EF}{1-EF}\right) \right] \right] \end{aligned} \quad (A11)$$

$$\lambda_1(t_1) = 0, \quad (A12)$$

$$\frac{d\lambda_2}{dt} = \frac{1}{h} \left[\frac{2R_q^{-1}(q - q_{SL})}{\rho} - \frac{2\lambda_2 \theta G_* e^{-\varphi h}}{gh\delta_{\theta}} - \frac{0.2\lambda_2 e^R f(Ri)U(T-T_a)}{\delta_{\theta}} \left(1 + \frac{0.07EF}{1-EF}\right) \right], \quad (A13)$$

$$\lambda_2(t_1) = 0, \quad (A14)$$

$$\begin{aligned} EF_i = \frac{1}{2B_{EF}^{-1}} \int_{t_0}^{t_1} & \left[\frac{0.07\lambda_1 \theta \rho c_p e^R f(Ri)U(T-T_a)}{(1-EF)^2} \left(\frac{0.2}{\delta_{\theta}}\right) + \frac{0.07\lambda_2 \rho q e^R f(Ri)U(T-T_a)}{(1-EF)^2} \left(\frac{0.2}{\delta_{\theta}}\right) \right. \\ & \left. + \frac{\lambda_2 \rho c_p e^R f(Ri)U(T-T_a)}{L_v(1-EF)^2} + \frac{0.07\lambda_2 \rho \delta_q e^R f(Ri)U(T-T_a)}{(1-EF)^2} \left(\frac{0.2}{\delta_{\theta}}\right) \right] dt + EF'_i \end{aligned} \quad (A15)$$

$$\begin{aligned} R = \frac{1}{2B_R^{-1}} \sum \int_{t_0}^{t_1} & \left[\left(1 + \frac{0.07EF}{1-EF}\right) \frac{0.2\lambda_1 \theta \rho c_p e^R f(Ri)U(T-T_a)}{\delta_{\theta}} + 1.32\lambda_1 \rho c_p e^R f(Ri)U(T-T_a) + (1 + \right. \\ & \left. \frac{0.07EF}{1-EF}) \frac{0.2\lambda_2 \rho q e^R f(Ri)U(T-T_a)}{\delta_{\theta}} + \frac{EF\lambda_2 \rho c_p e^R f(Ri)U(T-T_a)}{(1-EF)L_v} + \left(1 + \frac{0.07EF}{1-EF}\right) \frac{0.2\lambda_2 \rho \delta_q e^R f(Ri)U(T-T_a)}{\delta_{\theta}} \right] dt + R'. \end{aligned} \quad (A16)$$

References

1. McCabe, M.F.; Wood, E.F. Scale influences on the remote estimation of evapotranspiration using multiple satellite sensors. *Remote Sens. Environ.* **2006**, *105*, 271–285. [[CrossRef](#)]

2. Lu, Y.; Dong, J.; Steele-Dunne, S.C.; van de Giesen, N. Estimating surface turbulent heat fluxes from land surface temperature and soil moisture observations using the particle batch smoother. *Water Resour. Res.* **2016**, *52*, 9086–9108. [\[CrossRef\]](#)
3. Alfieri, J.; Kustas, W.P.; Prueger, J.H.; Chavez, J.L.; Evett, S.R.; Neals, C.; Anderson, M.; Hipps, L.; Copeland, K.; Howell, T.; et al. A comparison of the eddy covariance and lysimetry-based measurements of the surface energy fluxes during BEAREX08. *Int. Assoc. Hydrol. Sci.* **2012**, *352*, 215–218.
4. Liu, S.M.; Xu, Z.W.; Zhu, Z.L.; Jia, Z.Z.; Zhu, M.J. Measurements of evapotranspiration from eddy-covariance systems and large aperture scintillometers in the Hai River Basin, China. *J. Hydrol.* **2013**, *487*, 24–38. [\[CrossRef\]](#)
5. Gebler, S.; Hendricks Franssen, H.-J.; Putz, T.; Post, H.; Schmidt, M.; Vereecken, H. Actual evapotranspiration and precipitation measured by lysimeters: A comparison with eddy covariance and tipping bucket. *Hydrol. Earth Syst. Sci.* **2015**, *19*, 2145–2161. [\[CrossRef\]](#)
6. Hirschi, M.; Michel, D.; Lehner, I.; Seneviratne, S.I. A site-level comparison of lysimeter and eddy covariance flux measurements of evapotranspiration. *Hydrol. Earth Syst. Sci.* **2017**, *21*, 1809–1825. [\[CrossRef\]](#)
7. Moorhead, J.E.; Marek, G.W.; Colaizzi, P.D.; Gowda, P.H.; Evett, S.R.; Brauer, D.K.; Marek, T.H.; Porter, D.O. Evaluation of sensible heat flux and evapotranspiration estimates using a surface layer scintillometer and a large weighing lysimeter. *Sensors* **2017**, *17*, 2350.
8. Baldocchi, D.; Falge, E.; Gu, L.H.; Olson, R. FLUXNET: A new tool to study the temporal and spatial variability of ecosystem-scale carbon dioxide, water vapor, and energy flux densities. *Bull. Am. Meteorol. Soc.* **2001**, *82*, 2415–2434. [\[CrossRef\]](#)
9. Li, X.; Cheng, G.D.; Liu, S.M.; Xiao, Q.; Ma, M.G.; Jin, R.; Che, T.; Liu, Q.; Wang, W.; Wen, J.; et al. Heihe watershed allied telemetry experimental research (HiWATER): Scientific objectives and experimental design. *Bull. Am. Meteorol. Soc.* **2013**, *94*, 1145–1160. [\[CrossRef\]](#)
10. Xu, T.; Bateni, S.M.; Liang, S. Estimating turbulent heat fluxes with a weak-constraint data assimilation scheme: A case study (HiWATER-MUSOEXE). *IEEE Geosci. Remote Sens. Lett.* **2015**, *12*, 68–72.
11. Liu, S.; Li, X.; Xu, Z.; Che, T.; Xiao, Q.; Ma, M.; Liu, Q.; Jin, R.; Guo, J.; Wang, L.; et al. The Heihe integrated observatory network: A basin-scale land surface processes observatory in China. *Vadose Zone J.* **2018**, *17*, 180072. [\[CrossRef\]](#)
12. Bastiaanssen, W.G.M.; Menenti, M.; Feddes, R.A.; Holtslang, A.A.M. A remote sensing surface energy balance algorithm for land (SEBAL) 1. Formulation. *J. Hydrol.* **1998**, *212*, 198–212. [\[CrossRef\]](#)
13. Bastiaanssen, W.G.M.; Pelgrum, H.; Wang, J.; MA, Y.; Moreno, J.F.; Roenink, G.J.; Van Der Wal, T. A remote sensing surface energy balance algorithm for land (SEBAL) 2. Validation. *J. Hydrol.* **1998**, *212*, 213–229. [\[CrossRef\]](#)
14. Kalma, J.D.; McVicar, T.R.; McCabe, M.F. Estimating land surface evaporation: A review of methods using remotely sensed surface temperature data. *Surv. Geophys.* **2008**, *29*, 421–469. [\[CrossRef\]](#)
15. Allen, R.; Irmak, A.; Trezza, R.; Hendrickx, J.M.H.; Bastiaanssen, W.; Kjaersgaard, J. Satellite-based ET estimation in agriculture using SEBAL and METRIC. *Hydrol. Process.* **2011**, *25*, 4011–4027. [\[CrossRef\]](#)
16. Yilmaz, M.T.; Anderson, M.C.; Zaitchik, B.; Hain, C.R.; Crow, W.T.; Ozdogan, M.; Chun, J.A.; Evans, J. Comparison of prognostic and diagnostic surface flux modeling approaches over the Nile River basin. *Water Resour. Res.* **2014**, *50*, 386–408. [\[CrossRef\]](#)
17. Nishida, K.; Nemani, R.R.; Running, S.W.; Glassy, J.M. An operational remote sensing algorithm of land surface evaporation. *J. Geophys. Res. Atmos.* **2003**, *108*, 4270. [\[CrossRef\]](#)
18. Wang, K.; Li, Z.; Cribb, M. Estimating of evaporative fraction from a combination of day and night land surface temperature and NDVI: A new method to determine the Priestley-Taylor parameter. *Remote Sens. Environ.* **2006**, *102*, 293–305. [\[CrossRef\]](#)
19. Carlson, T. An overview of the “triangle method” for estimating surface evapotranspiration and soil moisture from satellite imagery. *Sensors* **2007**, *7*, 1612–1629. [\[CrossRef\]](#)
20. Stisen, S.; Sandholt, I.; Nørgaard, A.; Fensholt, R.; Jensen, K.H. Combining the triangle method with thermal inertia to estimate regional evapotranspiration—Applied to MSG-SEVIRI data in the Senegal River basin. *Remote Sens. Environ.* **2008**, *112*, 1242–1255. [\[CrossRef\]](#)
21. Tang, R.; Li, Z.-L.; Tang, B. An application of the Ts-VI triangle method with enhanced edges determination for evapotranspiration estimation from MODIS data in arid and semi-arid regions: Implementation and validation. *Remote Sens. Environ.* **2010**, *114*, 540–551. [\[CrossRef\]](#)

22. Sun, L.; Liang, S.; Yuan, W.; Chen, Z. Improving a Penman-Monteith evapotranspiration model by incorporating soil moisture control on soil evaporation in semiarid areas. *Int. J. Digit. Earth* **2013**, *6*, 134–156. [[CrossRef](#)]
23. Martínez Pérez, J.Á.; García-Galiano, S.G.; Martín-Gorriz, B.; Baille, A. Satellite-Based Method for Estimating the Spatial Distribution of Crop Evapotranspiration: Sensitivity to the Priestley-Taylor Coefficient. *Remote Sens.* **2017**, *9*, 611. [[CrossRef](#)]
24. Majazi, N.P.; Mannaerts, C.M.; Ramoelo, A.; Mathieu, R.; Mudau, A.E.; Verhoef, W. An intercomparison of satellite-based daily evapotranspiration estimates under different eco-climatic regions in south Africa. *Remote Sens.* **2017**, *9*, 307. [[CrossRef](#)]
25. Carlson, T.N.; Petropoulos, G.P. A new method for estimating of evapotranspiration and surface soil moisture from optical and thermal infrared measurements: The simplified triangle. *Int. J. Remote Sens.* **2019**, *40*, 7716–7729. [[CrossRef](#)]
26. Zhu, W.; Jia, S.; Lv, A. A universal Ts-VI triangle method for the continuous retrieval of evaporative fraction from MODIS products. *J. Geophys. Res. Atmos.* **2017**, *122*, 206–227. [[CrossRef](#)]
27. Zhang, H.; Gorelick, S.M.; Avisse, N.; Tilmant, A.; Rajsekhar, D.; Yoon, J. A New Temperature-Vegetation Triangle Algorithm with Variable Edges (TAVE) for Satellite-Based Actual Evapotranspiration Estimation. *Remote Sens.* **2016**, *8*, 735. [[CrossRef](#)]
28. Sousa, D.; Small, C. Spectral Mixture Analysis as a Unified Framework for the Remote Sensing of Evapotranspiration. *Remote Sens.* **2018**, *10*, 1961. [[CrossRef](#)]
29. Su, Z. The surface energy balance system (SEBS) for estimation of turbulent heat fluxes. *Hydrol. Earth Syst. Sci.* **2002**, *6*, 85–100. [[CrossRef](#)]
30. Liu, S.M.; Hu, G.; Lu, L.; Mao, D.F. Estimation of regional evapotranspiration by TM/ETM + data over heterogeneous surfaces. *Photogramm. Eng. Remote Sens.* **2007**, *73*, 1169–1178. [[CrossRef](#)]
31. Jia, L.; Xi, G.; Liu, S.; Huang, C.; Yan, Y.; Liu, G. Regional estimation of daily to annual regional evapotranspiration with MODIS data in the Yellow River Delta wetland. *Hydrol. Earth Syst. Sci.* **2009**, *13*, 1775–1787. [[CrossRef](#)]
32. Kustas, W.P.; Alfieri, J.G.; Anderson, M.C.; Colaizzi, P.D.; Prueger, J.H.; Evett, S.R.; Christopher, M.U.; Andrew, N.F.; Lawrence, E.H.; Jose, L.C.; et al. Evaluating the two-source energy balance model using local thermal and surface flux observations in a strongly advective irrigated agricultural area. *Adv. Water Resour.* **2012**, *50*, 120–133. [[CrossRef](#)]
33. Ma, W.; Hafeez, M.; Rabbani, U.; Ishikawa, H.; Ma, Y. Retrieved actual ET using SEBS model from Landsat-5 TM data for irrigation area of Australia. *Atmos. Environ.* **2012**, *59*, 408–414. [[CrossRef](#)]
34. Ma, Y.F.; Liu, S.M.; Zhang, F.; Zhou, J.; Jia, Z.Z.; Song, L.S. Estimations of regional surface energy fluxes over heterogeneous oasisdesert surfaces in the middle reaches of the Heihe River during HiWATER-MUSOEXE. *IEEE Geosci. Remote Sens. Lett.* **2015**, *12*, 671–675.
35. Song, L.S.; Kustas, W.P.; Liu, S.M.; Colaizzi, P.D.; Nieto, H.; Xu, Z.W.; Ma, Y.; Li, M.; Xu, T.; Agam, N.; et al. Applications of a thermal-based two-source energy balance model using Priestley-Taylor approach for surface temperature partitioning under advective conditions. *J. Hydrol.* **2016**, *540*, 574–587. [[CrossRef](#)]
36. Mallick, K.; Jarvis, A.J.; Fisher, J.B.; Tu, K.P.; Boegh, E.; Niyogi, D. Latent heat flux and canopy conductance based on Penman-Monteith, Priestly-Taylor equation, and Bouchets complementary hypothesis. *J. Hydrometeorol.* **2013**, *14*, 419–442. [[CrossRef](#)]
37. Mallick, K.; Jarvis, A.J.; Boegh, E.; Fisher, J.B.; Drewry, D.T.; Tu, K.P.; Hook, S.J.; Hulley, G.; Ardö, J.; Beringer, J.; et al. A surface temperature initiated closure (STIC) for surface energy balance fluxes. *Remote Sens. Environ.* **2014**, *141*, 243–261. [[CrossRef](#)]
38. Raoufi, R.; Beighley, E. Estimating Daily Global Evapotranspiration Using Penman-Monteith Equation and Remotely Sensed Land Surface Temperature. *Remote Sens.* **2017**, *9*, 1138. [[CrossRef](#)]
39. Peters-Lidard, C.D.; Kumar, S.V.; Mocko, D.M.; Tian, Y. Estimating evapotranspiration with land data assimilation systems, hydrological processes. *Hydrol. Process.* **2011**, *25*, 3979–3992. [[CrossRef](#)]
40. Xia, Y.; Sheffield, J.S.; Ek, M.B.; Dong, J.; Chaney, N.; Wei, H.; Meng, J.; Wood, E.F. Evaluation of multi-model simulated soil moisture in NLDAS-2. *J. Hydrol.* **2014**, *512*, 107–125. [[CrossRef](#)]
41. Xia, Y.; Ek, M.; Mocko, D.; Peters-Lidard, C.; Sheffield, J.; Dong, J.; Wood, E. Uncertainties, correlations, and optimal blends of drought indices from the NLDAS multiple land surface model ensemble. *J. Hydrometeorol.* **2014**, *15*, 1636–1650. [[CrossRef](#)]

42. Bateni, S.M.; Entekhabi, D. Surface heat flux estimation with the ensemble Kalman smoother: Joint estimation of state and parameters. *Water Resour. Res.* **2012**, *48*, W08521. [[CrossRef](#)]
43. Carrera, M.; Belair, S.; Bilodeau, B. The Canadian Land Data Assimilation System (CaLDAS): Description and synthetic evaluation study. *J. Hydrometeorol.* **2015**, *16*, 1293–1314. [[CrossRef](#)]
44. Xu, T.; Bateni, S.M.; Neale, C.M.U.; Auligne, T.; Liang, S. Estimation of turbulent heat fluxes by assimilation of land surface temperature observations from GOES satellites into an ensemble Kalman smoother framework. *J. Geophys. Res. Atmos.* **2018**, *123*, 2409–2423. [[CrossRef](#)]
45. Caparrini, F.; Castelli, F.; Entekhabi, D. Mapping of land-atmosphere heat fluxes and surface parameters with remote sensing data. *Bound. Layer Meteorol.* **2003**, *107*, 605–633. [[CrossRef](#)]
46. Caparrini, F.; Castelli, F.; Entekhabi, D. Estimation of surface turbulent fluxes through assimilation of radiometric surface temperature sequences. *J. Hydrometeorol.* **2004**, *5*, 145–159. [[CrossRef](#)]
47. Caparrini, F.; Castelli, F.; Entekhabi, D. Variational estimation of soil and vegetation turbulent transfer and heat flux parameters from sequences of multisensor imagery. *Water Resour. Res.* **2004**, *40*, 1713–1722. [[CrossRef](#)]
48. Bateni, S.M.; Entekhabi, D. Relative efficiency of land surface energy balance components. *Water Resour. Res.* **2012**, *48*, W04510. [[CrossRef](#)]
49. Bateni, S.M.; Entekhabi, D.; Jeng, D.-S. Variational assimilation of land surface temperature and the estimation of surface energy balance components. *J. Hydrol.* **2013**, *481*, 143–156. [[CrossRef](#)]
50. Bateni, S.M.; Entekhabi, D.; Castelli, F. Mapping evaporation and estimation of surface control of evaporation using remotely sensed land surface temperature from a constellation of satellites. *Water Resour. Res.* **2013**, *49*, 950–968. [[CrossRef](#)]
51. Bateni, S.M.; Entekhabi, D.; Margulis, S.; Castelli, F.; Kergoat, L. Coupled estimation of surface heat fluxes and vegetation dynamics from remotely sensed land surface temperature and fraction of photosynthetically active radiation. *Water Resour. Res.* **2014**, *50*, 8420–8440. [[CrossRef](#)]
52. Xu, T.; Bateni, S.M.; Margulis, S.A.; Song, L.; Lio, S. Partitioning evapotranspiration into soil evaporation and canopy transpiration via a two-source variational data assimilation system. *J. Hydrometeorol.* **2016**, *17*, 2353–2370. [[CrossRef](#)]
53. Xu, T.; He, X.; Bateni, S.M.; Auligne, T.; Liu, S.; Xu, Z.; Zhou, J.; Mao, K. Mapping regional turbulent heat fluxes via variational assimilation of land surface temperature data from polar orbiting satellites. *Remote Sens. Environ.* **2019**, *221*, 444–461. [[CrossRef](#)]
54. Abdolghafoorian, A.; Farhadi, L. Uncertainty quantification in land surface hydrologic modeling: Toward an integrated variational data assimilation framework. *IEEE J. Sel. Top. Appl. Earth Obs. Remote Sens.* **2016**, *9*, 2628–2637. [[CrossRef](#)]
55. Abdolghafoorian, A.; Farhadi, L.; Bateni, S.M.; Margulis, S.; Xu, T. Characterizing the effect of vegetation dynamics on the bulk heat transfer coefficient to improve variational estimation of surface turbulent fluxes. *J. Hydrometeorol.* **2017**, *18*, 321–333. [[CrossRef](#)]
56. He, X.; Xu, T.; Bateni, S.M.; Neale, C.M.U.; Auligne, T.; Liu, S.; Wang, K.; Mao, K.; Yao, Y. Evaluation of the Weak Constraint Data Assimilation Approach for estimating Turbulent Heat Fluxes at Six Sites. *Remote Sens.* **2018**, *10*, 1994. [[CrossRef](#)]
57. Crow, W.T.; Kustas, W.P. Utility of assimilating surface radiometric temperature observations for evaporative fraction and heat transfer coefficient retrieval. *Bound. Layer Meteorol.* **2005**, *115*, 105–130. [[CrossRef](#)]
58. Xu, T.; Bateni, S.M.; Liang, S.; Entekhabi, D.; Mao, K. Estimation of surface turbulent heat fluxes via variational assimilation of sequences of land surface temperatures from Geostationary Operational Environmental Satellites. *J. Geophys. Res. Atmos.* **2014**, *119*, 10780–10798. [[CrossRef](#)]
59. Sini, F.; Boni, G.; Caparrini, F.; Entekhabi, D. Estimation of large-scale evaporation fields based on assimilation of remotely sensed land temperature. *Water Resour. Res.* **2008**, *44*, W06410. [[CrossRef](#)]
60. Abdolghafoorian, A.; Farhadi, L. Estimation of surface turbulent fluxes from land surface moisture and temperature via a variational data assimilation framework. *Water Resour. Res.* **2019**, *55*. [[CrossRef](#)]
61. Mahfouf, J.-F. Analysis of soil moisture from near-surface parameters: A feasibility study. *J. Appl. Meteorol.* **1991**, *30*, 1534–1547. [[CrossRef](#)]
62. Bouttier, F.; Mahfouf, J.F.; Noilhan, J. Sequential assimilation of soil moisture from atmospheric low-level parameters. Part I: Sensitivity and calibration studies. *J. Appl. Meteorol.* **1993**, *32*, 1335–1351. [[CrossRef](#)]

63. Bouttier, F.; Mahfouf, J.F.; Noilhan, J. Sequential assimilation of soil moisture from atmospheric low-level parameters. II: Implementation in a mesoscale model. *J. Appl. Meteorol.* **1993**, *32*, 1352–1364. [\[CrossRef\]](#)
64. Mahfouf, J.-F.; Viterbo, P.; Douville, H.; Beljaars, A.; Saarinen, S. A Revised land-surface analysis scheme in the Integrated Forecasting System. *ECMWF Newsl.* **2000**, *88*, 8–13.
65. Mahfouf, J.-F.; Bergaoui, K.; Draper, C.; Bouyssel, F.; Taillefer, F.; Taseva, L. A comparison of two off-line soil analysis schemes for assimilation of screen level observations. *J. Geophys. Res.* **2009**, *114*, D08105. [\[CrossRef\]](#)
66. Douville, H.; Viterbo, P.; Mahfouf, J.F.; Beljaars, A.C. Evaluation of the optimum interpolation and nudging techniques for soil moisture analysis using FIFE data. *Mon. Weather Rev.* **2000**, *128*, 1733–1756. [\[CrossRef\]](#)
67. Hess, R. Assimilation of screen-level observations by variational soil moisture analysis. *Meteorol. Atmos. Phys.* **2001**, *77*, 145–154. [\[CrossRef\]](#)
68. Drusch, M.; Viterbo, P. Assimilation of screen-level variables in ECMWF's integrated forecast system: A study on the impact on the forecast quality and analyzed soil moisture. *Mon. Weather Rev.* **2007**, *135*, 300–314. [\[CrossRef\]](#)
69. De Rosnay, P.; Drusch, M.; Vasiljevic, D.; Balsamo, G.; Albergel, C.; Isaksen, L. A simplified Extended Kalman Filter for the global operational soil moisture analysis at ECMWF. *Q. J. R. Meteorol. Soc.* **2013**, *139*, 1199–1213. [\[CrossRef\]](#)
70. Ren, D.; Xue, M. Retrieval of land surface model state variables through assimilating screen level humidity and temperature measurements. *Adv. Meteorol.* **2016**. [\[CrossRef\]](#)
71. De Lannoy, G.J.M.; de Rosnay, P.; Reichle, R.H. Soil Moisture Data Assimilation. In *Handbook of Hydrometeorological Ensemble Forecasting*; Duan, Q., Pappenberger, F., Eds.; Springer: Berlin/Heidelberg, Germany, 2016.
72. Holtslag, A.A.M.; Van Ulden, A.P. A single scheme for daytime estimates of the surface fluxes from routine weather data. *J. Clim. Appl. Meteorol.* **1983**, *22*, 517–529. [\[CrossRef\]](#)
73. Margulis, S.A.; Entekhabi, D. A coupled land surface-boundary layer model and its adjoint. *J. Hydrometeorol.* **2001**, *2*, 274–296. [\[CrossRef\]](#)
74. Alapaty, K.; Seaman, N.L.; Niyogi, D.S.; Hanna, A.F. Assimilating surface data to improve the accuracy of atmospheric boundary layer simulations. *J. Appl. Meteorol.* **2001**, *40*, 2068–2082. [\[CrossRef\]](#)
75. Balsamo, G.; Mahfouf, J.F.; Belair, S.; Deblonde, G. A land data assimilation system for soil moisture and temperature: An information content study. *J. Hydrometeorol.* **2007**, *8*, 1225–1242. [\[CrossRef\]](#)
76. Shang, K.Z.; Wang, S.G.; Ma, Y.X.; Zhou, Z.J.; Wang, J.Y.; Liu, H.L.; Wang, Y.Q. A scheme for calculating soil moisture content by using routine weather data. *Atmos. Chem. Phys.* **2007**, *7*, 5197–5206. [\[CrossRef\]](#)
77. Salvucci, G.D.; Gentine, P. Emergent relation between surface vapor conductance and relative humidity profiles yields evaporation rates from weather data. *Proc. Natl. Acad. Sci. USA* **2013**, *110*, 6287–6291. [\[CrossRef\]](#)
78. Rigden, A.J.; Salvucci, G.D. Evapotranspiration based on equilibrated relative humidity (ETRHEQ): Evaluation over the continental U.S. *Water Resour. Res.* **2015**, *51*, 2951–2973. [\[CrossRef\]](#)
79. Gentine, P.; Chhang, A.; Rigden, A.; Salvucci, G. Evaporation estimates using weather station data and boundary layer theory. *Geophys. Res. Lett.* **2016**, *43*, 661–670. [\[CrossRef\]](#)
80. Lum, M.; Bateni, S.M.; Shiri, J.; Keshavarzi, A. Estimation of reference evapotranspiration from climatic data. *Int. J. Hydrol.* **2017**, *1*. [\[CrossRef\]](#)
81. Tajfar, E.; Bateni, S.M.; Margulis, S.A.; Gentine, P.; Auligne, T. Estimation of Turbulent Heat Fluxes via Assimilation of Air Temperature and Specific Humidity into an Atmospheric Boundary Layer Model. *J. Hydrometeorol.* **2020**, *21*, 205–225. [\[CrossRef\]](#)
82. Bateni, S.M.; Liang, S. Estimating surface energy fluxes using a dual-source data assimilation approach adjoined to the heat diffusion equation. *J. Geophys. Res.* **2012**, *117*, D17118. [\[CrossRef\]](#)
83. Tajfar, E.; Bateni, S.M.; Lakshmi, V.; Ek, M. Estimation of surface heat fluxes via variational assimilation of land surface temperature, air temperature and specific humidity into a coupled land surface-atmospheric boundary layer model. *J. Hydrol.* **2020**. [\[CrossRef\]](#)
84. Kustas, W.P.; Choudhury, B.J.; Moran, M.S.; Reginato, R.J.; Jackson, R.D.; Gay, L.W.; Weaver, H.L. Determination of sensible heat flux over sparse canopy using thermal infrared data. *Agric. For. Meteorol.* **1989**, *44*, 197–216. [\[CrossRef\]](#)
85. Brutsaert, W.; Sugita, M. The Extent of the Unstable Monin-Obukhov Layer for Temperature and Humidity Above Complex Hilly Grassland. *Bound. Layer Meteorol.* **1990**, *51*, 383–400. [\[CrossRef\]](#)

86. Mahrt, L.; Vickers, D. Boundary-layer adjustment over small-scale changes of surface heat flux. *Bound. Layer Meteorol.* **2015**, *116*, 313–330. [[CrossRef](#)]
87. Yang, R.; Friedl, M.A. Determination of roughness lengths for heat and momentum over boreal forests. *Bound. Layer Meteorol.* **2003**, *107*, 581–603. [[CrossRef](#)]
88. Timmermans, J.; Su, Z.; van der Tol, C.; Verhoef, A.; Verhoef, W. Quantifying the uncertainty in estimates of surface–atmosphere fluxes through joint evaluation of the SEBS and SCOPE models. *Hydrol. Earth Syst. Sci.* **2013**, *17*, 1561–1573. [[CrossRef](#)]
89. Crago, R.D.; Brutsaert, W. Daytime evaporation and self-preservation of the evaporative fraction and the Bowen ratio. *J. Hydrol.* **1996**, *178*, 241–255. [[CrossRef](#)]
90. Garcia, J.R.; Mellado, J.P. The two-layer structure of the entrainment zone in the convective boundary layer. *J. Atmos. Sci.* **2014**, *71*, 1935–1955. [[CrossRef](#)]
91. Gentine, P.; Bellon, G.; van Heerwaarden, C.C. A closer look at boundary layer inversion in large-eddy simulations and bulk models: Buoyance-driven case. *J. Atmos. Sci.* **2015**, *72*, 728–749. [[CrossRef](#)]
92. Shuttleworth, W.J. *Terrestrial Hydrometeorology*; John Wiley & Sons: Hoboken, NJ, USA, 2012.
93. Beljaars, A.; Holtslag, B. Flux parameterization over land surfaces for atmospheric models. *J. Appl. Meteorol.* **1991**. [[CrossRef](#)]
94. Brubaker, K.L.; Entekhabi, D. An analytic approach to modeling the land-atmosphere interaction: 1. Construct and equilibrium behavior. *Water Resour. Res.* **1995**, *31*, 619–632. [[CrossRef](#)]
95. Kim, C.P.; Entekhabi, D. Impact of soil heterogeneity in a mixed-layer model of the planetary boundary layer. *Hydrol. Sci.* **1998**, *43*, 633–658. [[CrossRef](#)]
96. Kim, C.P.; Entekhabi, D. Feedbacks in the Land-Surface and Mixed-Layer Energy Budgets. *Bound. Layer Meteorol.* **1998**, *88*, 1–21. [[CrossRef](#)]
97. Smeda, M.S. A bulk model for the atmospheric planetary boundary layer. *Bound. Layer Meteorol.* **1979**, *17*, 411–428. [[CrossRef](#)]
98. Kim, C.P.; Entekhabi, D. Examination of two methods for estimating regional evaporation using a coupled mixed layer and land surface mode. *Water Resour. Res.* **1997**, *33*, 2109–2116. [[CrossRef](#)]
99. Bagley, J.E.; Desai, A.R.; West, P.C.; Foley, J.A. A simple, minimal parameter model for predicting the influence of changing land cover on the land-atmosphere system. *Earth Interact.* **2011**, *15*, 1–32. [[CrossRef](#)]
100. Margulis, S.A.; Entekhabi, D. Variational assimilation of radiometric surface temperature and reference-level micrometeorology into a model of the atmospheric boundary layer and land surface. *Mon. Weather Rev.* **2003**, *131*, 1272–1288. [[CrossRef](#)]
101. Stull, R.B. *An Introduction to Boundary Layer Meteorology*; Springer: Berlin/Heidelberg, Germany, 2012.
102. Gentine, P.; Entekhabi, D.; Chehbouni, A.; Boulet, G.; Duchemin, B. Analysis of evaporative fraction diurnal behavior. *Agric. For. Meteorol.* **2007**, *143*, 13–29. [[CrossRef](#)]
103. Liang, S.; Zhao, X.; Yuan, W.; Liu, S.; Cheng, X.; Xiao, Z.; Zhang, X.; Liu, Q.; Cheng, J.; Tang, H.; et al. A long-term Global Land Surface Satellite (GLASS) dataset for environmental studies. *Int. J. Digit. Earth* **2013**, *6*, 5–33. [[CrossRef](#)]
104. Xiao, Z.Q.; Liang, S.; Wang, J.D.; Chen, P.; Yin, X.J.; Zhang, L.Q.; Song, J.L. Use of general regression neural networks for generating the GLASS leaf area index product from time-series MODIS surface reflectance. *IEEE Trans. Geosci. Remote Sens.* **2014**, *52*, 209–223. [[CrossRef](#)]
105. Li, X.; Liu, S.M.; Xiao, Q.; Ma, M.G.; Jin, R.; Che, T.; Wang, W.Z.; Hu, X.L.; Xu, Z.W.; Wen, J.G.; et al. A multiscale dataset for understanding complex eco-hydrological processes in a heterogeneous oasis system. *Sci. Data* **2017**, *4*. [[CrossRef](#)] [[PubMed](#)]
106. Xu, T.R.; Guo, Z.X.; Liu, S.M.; He, X.L.; Meng, Y.F.Y.; Xu, Z.W.; Xia, Y.L.; Xiao, J.F.; Zhang, Y.; Ma, Y.F.; et al. Evaluating Different Machine Learning Methods for Upscaling Evapotranspiration from Flux Towers to the Regional Scale. *J. Geophys. Res. Atmos.* **2018**, *123*, 8674–8690. [[CrossRef](#)]
107. Flerchinger, G.N.; Reba, M.L.; Marks, D. Measurement of surface energy fluxes from two Rangeland sites and comparison with a multilayer canopy model. *J. Hydrometeorol.* **2012**, *13*, 1038–1051. [[CrossRef](#)]
108. Radic, V.; Menounos, B.; Shea, J.; Fitzpatrick, N.; Tessema, M.A.; Dery, S.J. Evaluation of different methods to model near-surface turbulent fluxes for a mountain glacier in the Cariboo Mountains, BC, Canada. *Cryosphere* **2017**, *11*, 2897–2918. [[CrossRef](#)]
109. Shokri, N.; Lehmann, P.; Vontobel, P.; Or, D. Drying front and water content dynamics during evaporation from sand delineated by neutron radiography. *Water Resour. Res.* **2008**, *44*, W06418. [[CrossRef](#)]

110. Xu, T.R.; Liu, S.M.; Xu, Z.W.; Liang, S.; Xu, L. A dual-pass data assimilation scheme for estimating surface fluxes with FY3A-VIRR land surface temperature. *Sci. China Earth Sci.* **2015**, *58*, 211–230. [[CrossRef](#)]
111. Garratt, J.R. *The Atmospheric Boundary Layer*; Cambridge University Press: Cambridge, UK, 1994.
112. Brutsaert, W. *Hydrology: An Introduction*; Cambridge University Press: Cambridge, UK, 2005.



© 2020 by the authors. Licensee MDPI, Basel, Switzerland. This article is an open access article distributed under the terms and conditions of the Creative Commons Attribution (CC BY) license (<http://creativecommons.org/licenses/by/4.0/>).